

## Central and Non-central HBT from AGS to RHIC

Boris Tomášik and Urs Achim Wiedemann

*Theory Division, CERN, CH-1211 Geneva 23, Switzerland*

We review the status of particle interferometry in ultra-relativistic nucleus-nucleus collisions. The theoretical focus is on the model-independent space-time interpretation of HBT radius parameters and its extension to the geometrical and dynamical asymmetries generated in finite impact parameter collisions. On the experimental side, we give a complete account of all presently available data for beam energies above 2 AGeV. We discuss what these data imply for the dynamics and space-time extension of the collision region and for the condition under which particles decouple from this region.

**Contents**

1. Introduction	3
2. The Gaussian source formalism	5
2.1. Gaussian correlators in terms of space-time variances	6
2.2. Central (azimuthally symmetric) collisions	8
2.2.1. The Cartesian Bertsch-Pratt parametrisation	8
2.2.2. Interpretation of space-time variances	10
2.2.3. The Yano-Koonin-Podgoretskii parametrisation	11
2.3. Collisions at finite impact parameter	12
2.3.1. Choice of coordinate system	12
2.3.2. HBT radius parameters from space-time variances	13
2.3.3. Symmetries satisfied by space-time variances	14
2.3.4. Explicit azimuthal dependences at mid-rapidity	16
2.3.5. Implicit azimuthal dependence at mid-rapidity	18
2.3.6. Implicit azimuthal dependence at forward rapidity	22
2.3.7. Reconstruction of the reaction plane	24
3. Two-particle correlations from model calculations	25
3.1. Model parametrisations of the emission function	25
3.2. Hydrodynamic models	29
3.3. Monte Carlo event generators	31
4. HBT measurements	32
4.1. Coulomb final state corrections	32
4.2. Experiments at the Alternating Gradient Synchrotron (AGS)	36
4.3. Experiments at the CERN Super Proton Synchrotron (SPS)	38
4.4. Experiments at the Relativistic Heavy Ion Collider (RHIC)	45
4.5. Discussion of the data	46
4.5.1. Size and transverse momentum dependence of HBT radii	46
4.5.2. $R_o/R_s$	49
4.5.3. Average phase-space density	50
4.5.4. Energy and multiplicity dependence	54
4.5.5. Azimuthal dependence of HBT radius parameters	57
Acknowledgements	58
References	59

## 1. Introduction

One aspect in which a theory of high-energy nucleus-nucleus collisions has to go beyond conventional nuclear and high-energy physics is in understanding the space-time extension of the collision region and its collective dynamical evolution. On the microscopic level, basic quantities governing the reaction dynamics such as the probability that a particle can escape the collision region without further interaction (“freeze-out”) or that it participates in three-body interactions, clearly depend on the space-time extension of the collision region and the relative velocity of the particle with respect to the medium. On a macroscopic level, the study of the equation of state of hot and dense matter rests on assessing the energy density and pressure attained in nucleus-nucleus collisions. The operational definition of these quantities clearly involves the measurement of volumes and the determination of the degree of collectivity of the expansion.

It has been long recognised in both astrophysics<sup>34,35</sup> and particle physics<sup>27</sup> that correlations between identical bosons give access to the geometry of particle emitting sources. While statistical requirements for particle correlation measurements are significant, interferometric techniques are often the method of choice when conventional space-time measurement techniques (like paralaxe measurements or scattering with external probes) are not feasible. In the context of nucleus-nucleus collisions, the use of identical two-particle “Hanbury-Brown Twiss” (HBT) correlations was first forcefully advocated in the 1970s in a series of pioneering works published independently in the East<sup>51,52,77</sup> and the West<sup>21,31</sup>. Those were followed by the first detailed discussions of how to separate quantum interference effects from final state interactions<sup>32,53</sup>. By now, particle interferometry provides the most direct and most detailed space-time picture of the late stage of nucleus-nucleus collisions.

2 AGeV, the lowest beam energy delivered by the Alternating Gradient Synchrotron (AGS) at the Brookhaven National Laboratory (BNL), is a natural choice for the lowest energy included in a review on relativistic nucleus-nucleus collisions. Non-relativistic collisions at lower beam energies (up to several 100 AMeV) create evaporative sources with long lifetimes ( $\sim$  several 100 fm/c) which are dominated by proton and neutron emission. Strong final state effects dominate correlation measurements. A comprehensive review of the rather different physics at these lower energies exists<sup>12</sup>. Above 2 AGeV, pion abundances become important, source lifetimes are

much shorter ( $\sim 10$  fm/c) and quantum interference effects dominate over the strong (but not necessarily over the electro-magnetic) final state interactions. Moreover, the increase of pion multiplicity per event with increasing beam energy helps to overcome the major obstacle of particle interferometry at lower energies, namely the lack of statistics.

The increase in event multiplicity and the accumulation of increasing event samples lead throughout the 1990s to a rapid refinement of analysis tools. Early analyses often show “one-dimensional” two-particle correlators as functions of one relative momentum variable only. These were soon superseded by “three-dimensional” representations. Then, the increasing statistics allowed to resolve “three-dimensional” correlation functions with respect to the average transverse pair momentum and rapidity. Only recently, the next step of these refinements was taken when the first measurements of HBT with respect to the orientation of the reaction plane became available. Paralleling this experimental progress and sometimes anticipating it was a theoretical effort which related systematically these more and more differential interferometric measurements to more and more detailed geometrical and dynamical properties of the particle emitting source. By the end of the CERN SPS heavy ion program in 2000, several reviews<sup>100,37,25</sup> gave detailed summaries of these developments.

We were asked to contribute to the present review volume only two years later, at a time when HBT measurements from RHIC are published but no thorough theoretical analysis of these findings is yet available. In this situation, we decided to emphasise in a topical review those two aspects of particle interferometry which are likely to play an important role in the further discussion of RHIC data and which are not yet adequately represented in reviews. On the experimental side, our focus will be on a comprehensive overview of all data from AGS, SPS and RHIC. This is timely not only because several experiments at the AGS and SPS just finalised their HBT analyses. It is also of obvious use for a discussion of the energy-dependence of HBT correlation measurements which plays an important role in the HBT studies at RHIC. On the theoretical side, our presentation reflects the fact that the first measurements of azimuthally dependent HBT radius parameters in finite impact parameter collisions at AGS and RHIC became available after 1999. That these novel observables may provide a complementary space-time picture to the large elliptic flow measured at RHIC gives an additional motivation for discussing their theoretical basis

in detail.

This review is organised as follows: In section 2, we introduce the formalism for calculating identical two-particle correlations from particle emission functions. In particular, we discuss in detail the case of non-central collisions. In section 3, we briefly summarise models for the particle emitting source which have been used in calculating HBT correlations from ultra-relativistic heavy-ion collisions. Finally, in section 4, we give a complete account of the experimental situation and we discuss shortly the most important features of the presently available data. Since most data are for central collisions, readers primarily interested in the data summary may jump from the introductory sections 2.1 and 2.2 directly to section 4. The extension to non-central collisions in section 2.3 and the corresponding experimental overview in section 4.5.5 can be read independently. Also, the short overview of model calculations in section 3 allows for an independent reading.

## 2. The Gaussian source formalism

The two-particle momentum correlator between identical bosons with momenta  $p_1$  and  $p_2$  is defined as the quotient of two-particle and one-particle spectra<sup>a</sup>,

$$C(\mathbf{q}, \mathbf{K}) = \frac{\frac{d^6 N}{d\mathbf{p}_1^3 d\mathbf{p}_2^3}}{\frac{d^3 N}{d\mathbf{p}_1^3} \frac{d^3 N}{d\mathbf{p}_2^3}} . \quad (1)$$

Experimentally, this ratio is constructed for event samples, normalising *actual pairs* from the same event by *mixed pairs* from different events. Usually, the two-particle correlator is written in terms of the corresponding relative and average pair momenta

$$\mathbf{q} = \mathbf{p}_1 - \mathbf{p}_2 , \quad (2)$$

$$\mathbf{K} = \frac{1}{2} (\mathbf{p}_1 + \mathbf{p}_2) . \quad (3)$$

If the particle spectra entering (1) are corrected for final state interactions, then the two-particle correlator  $C(\mathbf{q}, \mathbf{K})$  is related to the emission function  $S(x, K)$ <sup>77,31,66,68,10,17</sup> which is the Wigner phase-space density of the

---

<sup>a</sup> Throughout this review, we use italics for four-vectors and bold for three-vectors.

particle emitting system

$$C(\mathbf{q}, \mathbf{K}) \approx 1 + \frac{|\int d^4x S(x, K) e^{iq \cdot x}|^2}{|\int d^4x S(x, K)|^2}. \quad (4)$$

For a derivation of (4) in different formalisms (coherent source formalism and Gaussian wave-packet formalism), we refer to the review<sup>100</sup>. Equation (4) is approximate since it is based on the smoothness approximation  $S(x, K - \frac{1}{2}q)S(y, K + \frac{1}{2}q) \approx S(x, K)S(y, K)$  valid for small relative momenta. Moreover, the following discussion of (4) will regularly employ the on-shell approximation  $K_0 \approx \sqrt{\mathbf{K}^2 + m^2}$  which neglects the off-shell components of  $K$ . Corrections to these approximations were studied systematically<sup>19</sup> and were found to be small except for especially constructed toy models whose phase-space volumes were very small (i.e. comparable to the lower bound coming from the Heisenberg uncertainty relation). For particle correlations in nucleus-nucleus collisions, equation (4) is a well-defined starting point. The emission function  $S(x, K)$  can be viewed as the probability that a particle with momentum  $K$  is emitted from the space-time point  $x$  in the collision region.

The aim of HBT two-particle interferometry is to extract from the experimentally measured correlator  $C(\mathbf{q}, \mathbf{K})$  as much information about  $S(x, K)$  as possible. This includes i) information about the geometrical extent of the collision region at the time of last hadronic scattering (freeze-out), ii) information about the freeze-out time and emission duration of the source, iii) information about the collective velocity of the expanding collision region in the directions parallel and orthogonal to the beam, iv) information about the azimuthal dependence of the geometrical and dynamical properties of the collision region in finite impact parameter collisions. From these primary measurements, various derived quantities can be extracted, in particular the particle phase-space density at freeze-out.

### 2.1. Gaussian correlators in terms of space-time variances

Experimental data of two-particle correlations are usually parametrised by a Gaussian ansatz in terms of HBT radius parameters  $R_{ij}(\mathbf{K})$  and the  $\lambda$ -intercept parameter

$$C(\mathbf{q}, \mathbf{K}) = 1 + \lambda(\mathbf{K}) \exp \left[ - \sum_{ij} R_{ij}^2(\mathbf{K}) \mathbf{q}_i \mathbf{q}_j \right]. \quad (5)$$

Here, the indices  $i, j$  run over three of the four components of  $q$ . The fourth component of  $q$  in (2) is fixed by the requirement that the final state particles are on-shell

$$q \cdot K = \frac{1}{2} (p_1^2 - p_2^2) = 0 \implies q_0 = \frac{\mathbf{K} \cdot \mathbf{q}}{K_0}. \quad (6)$$

Different choices of the three independent components of  $q = (q_0, \mathbf{q})$  correspond to different Gaussian parametrisations.

The connection between the HBT radius parameters and the space-time structure of the source is based on a Gaussian approximation to the emission function

$$S(x, K) \approx S(\bar{x}(K), K) \exp \left[ -\frac{1}{2} \tilde{x}^\mu(K) B_{\mu\nu}(K) \tilde{x}^\nu(K) \right]. \quad (7)$$

The space-time coordinates  $\tilde{x}_\mu$  in (7) are defined relative to the “effective source centre”  $\bar{x}(K)$  for bosons emitted with momentum  $\mathbf{K}$ <sup>18,43</sup>

$$\tilde{x}^\mu(K) = x^\mu - \bar{x}^\mu(K), \quad \bar{x}^\mu(K) = \langle x^\mu \rangle(K), \quad (8)$$

where  $\langle \dots \rangle$  denotes an average with the emission function  $S(x, K)$ :

$$\langle f \rangle(K) = \frac{\int d^4x f(x) S(x, K)}{\int d^4x S(x, K)}. \quad (9)$$

The choice

$$(B^{-1})_{\mu\nu}(K) = \langle \tilde{x}_\mu \tilde{x}_\nu \rangle(K) \quad (10)$$

ensures that the Gaussian ansatz (7) has the same rms widths in space-time as the full emission function. Inserting (7) into the basic relation (4), the correlator takes a Gaussian form,

$$C(\mathbf{q}, \mathbf{K}) = 1 + \exp [-q_\mu q_\nu \langle \tilde{x}^\mu \tilde{x}^\nu \rangle(\mathbf{K})]. \quad (11)$$

Since the correlator depends only on the relative distances  $\tilde{x}^\mu$  with respect to the source centre, no information can be obtained about the position  $\bar{x}(\mathbf{K})$  of the centre of the emission.

Finally, we comment on  $\lambda(\mathbf{K})$  in eq. (5) which parametrises the intercept of the correlation function for  $q = 0$ . This  $\lambda$ -parameter is unity for a chaotic source and it is smaller than 1 for a source with partially coherent particle emission. In practice, however, there are many other reasons why deviations from  $C(q = 0) = 2$  may be observed. For example, contributions to pion production<sup>96</sup> from long-lived resonances lead to an extended source

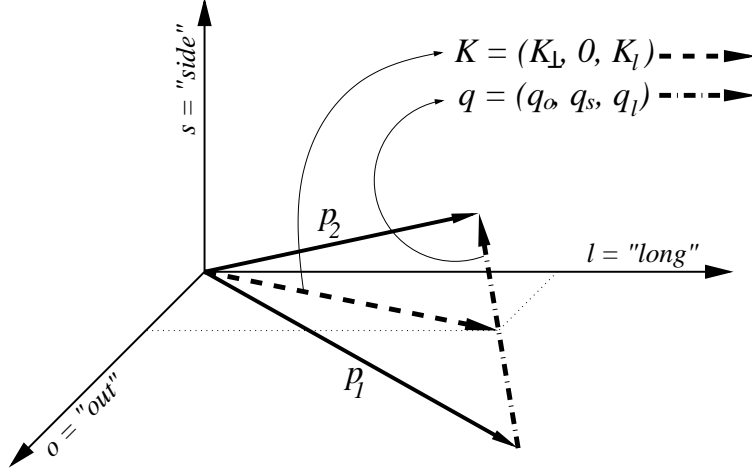


Fig. 1. The out-side-longitudinal *osl* coordinate system.

component which is reflected in a narrow peak of the correlation function. If this peak is narrower than the experimental resolution in relative momentum, a reduced intercept is observed. Also, misidentified particles in the sample of identical particle pairs reduce the correlation strength  $\lambda(\mathbf{K})$ . In addition to this, many technical details of the analysis – such as Coulomb correction or finite momentum resolution – can influence the value of  $\lambda$ .

## 2.2. Central (azimuthally symmetric) collisions

### 2.2.1. The Cartesian Bertsch-Pratt parametrisation

In the *out-side-longitudinal* (*osl*) coordinate system, defined in Fig. 1, the longitudinal (*long*) direction points along the beam axis. In the transverse plane, the *out* direction is chosen parallel to the transverse component of the pair momentum  $K_\perp$ , the remaining Cartesian component denotes the *side* direction. In this way, the out-axis is rotated independently for each particle pair. The azimuthal symmetry of the particle source in central collisions then translates in the *osl* coordinate system into a reflection symmetry with respect to the *side*-direction:

$$S(x, y, z, t; K_\perp, K_l) = S(x, -y, z, t; K_\perp, K_l). \quad (12)$$



This  $\tilde{y} \rightarrow -\tilde{y}$  symmetry translates to a  $q_s \rightarrow -q_s$  symmetry of the two-particle correlation function (11). The Cartesian Bertsch-Pratt parametrisation<sup>66,8,18</sup> exploits this reflection symmetry to write the two-particle correlator as

$$C(\mathbf{q}, \mathbf{K}) = \exp[-R_o^2(\mathbf{K}) q_o^2 - R_s^2(\mathbf{K}) q_s^2 - R_l^2(\mathbf{K}) q_l^2 - 2 R_{ol}^2(\mathbf{K}) q_o q_l]. \quad (13)$$

This parametrisation is based on the three Cartesian spatial components  $q_o$  (*out*),  $q_s$  (*side*),  $q_l$  (*long*) of the relative momentum  $q$ . The temporal component is eliminated via the mass-shell constraint (6)

$$q^0 = \boldsymbol{\beta} \cdot \mathbf{q}, \quad \boldsymbol{\beta} = (\beta_\perp, 0, \beta_l), \quad (14)$$

where  $\boldsymbol{\beta} = \mathbf{K}/K_0$ . To express the HBT radius parameters  $R_i^2(\mathbf{K})$  in terms of space-time variances  $\langle \tilde{x}_\mu \tilde{x}_\nu \rangle(K)$ , we insert the on-shell constraint  $q^0 = \boldsymbol{\beta} \cdot \mathbf{q}$  into the correlator (11), and compare the result with the Gaussian parametrisation (5) of the correlator. One then finds that the HBT radius parameters measure different combinations of the spatial and temporal extent of the collision system<sup>18,43</sup>:

$$R_s^2(K) = \langle \tilde{y}^2 \rangle(K), \quad (15)$$

$$R_o^2(K) = \langle (\tilde{x} - \beta_\perp \tilde{t})^2 \rangle(K), \quad (16)$$

$$R_l^2(K) = \langle (\tilde{z} - \beta_l \tilde{t})^2 \rangle(K), \quad (17)$$

$$R_{ol}^2(K) = \langle (\tilde{x} - \beta_\perp \tilde{t})(\tilde{z} - \beta_l \tilde{t}) \rangle(K), \quad (18)$$

$$R_{os}^2(K) = 0, \quad (19)$$

$$R_{sl}^2(K) = 0. \quad (20)$$

The  $y \rightarrow -y$  reflection symmetry of the emission function implies that the three space-time variances  $\langle \tilde{x}_\mu \tilde{x}_\nu \rangle(K)$  linear in  $\tilde{y}$  vanish. For the azimuthally symmetric case, there are only seven non-vanishing space-time variances which combine to four non-vanishing HBT-radius parameters  $R_{ij}^2(K)$ . This information is tabulated in the first column of Table 1.

In general, symmetries of the emission function translate into constraints for the space-time variances and thus lead to simpler expressions for the HBT radius parameters. Of particular relevance is the limit  $K_\perp \rightarrow 0$ . In this limit, no transverse vector allows to distinguish between the *out*- and *side*-components, and space-time variances thus become invariant under the exchange  $\tilde{x} \rightarrow \tilde{y}$ . This implies that  $\langle \tilde{x}^2 \rangle(K_\perp = 0) = \langle \tilde{y}^2 \rangle(K_\perp = 0)$ . Also,

the off-diagonal terms  $\langle \tilde{z}\tilde{x} \rangle(K_\perp = 0)$  and  $\langle \tilde{t}\tilde{x} \rangle(K_\perp = 0)$  vanish. As a consequence, the HBT radius parameters show the following limiting behaviour

$$\lim_{K_\perp \rightarrow 0} R_o^2(K) = \lim_{K_\perp \rightarrow 0} R_s^2(K), \quad (21)$$

$$\lim_{K_\perp \rightarrow 0} R_{ol}^2(K) = 0. \quad (22)$$

Further symmetries are sometimes helpful to gain physical intuition. For example, longitudinal boost-invariance implies a  $\tilde{z} \rightarrow -\tilde{z}$  reflection symmetry of the emission function which is approximately satisfied near mid-rapidity. This implies that the space-time variances linear in  $\tilde{z}$  vanish. In the longitudinally comoving system (LCMS)

$$\text{LCMS:} \quad \beta_l = 0, \quad (23)$$

this leads to the further simplifications  $R_l^2(K) = \langle \tilde{z}^2 \rangle(K)$  and  $R_{ol}^2(K) = 0$ .

### 2.2.2. Interpretation of space-time variances

The space-time variances  $\langle \tilde{x}_\mu \tilde{x}_\nu \rangle(K)$  depend on the pair momentum  $K$ . To understand their physical meaning, consider an observer who views a strongly expanding collision region. Some parts of the collision region move towards the observer and the particle spectrum emitted from those parts will appear blue-shifted. Other parts move away from the observer and appear red-shifted. Thus, if the observer looks at the collision system with a wavelength filter of some frequency, he sees only part of the collision region. Adopting a notion coined by Sinyukov, the observer sees a “region of homogeneity”. In HBT interferometry, the role of the wavelength filter is played by the pair momentum  $\mathbf{K}$ . The direction of  $\mathbf{K}$  corresponds to the direction from which the collision region is viewed. The modulus of  $\mathbf{K}$  characterises the central velocity  $\beta = \mathbf{K}/K_0$  of that part of the collision region which is seen through the wavelength filter. This situation is illustrated in Fig. 2. Depending on the direction and modulus of  $\mathbf{K}$ , different parts of the collision region are measured. The centre of a region of homogeneity  $\langle x_\mu \rangle$  depends on  $\mathbf{K}$  and lies typically between the center of the collision region and the observer. In the Gaussian approximation, the region of homogeneity is described by a four-dimensional space-time ellipsoid centered around  $\langle \tilde{x}_\mu \rangle(\mathbf{K})$  and characterised by  $S(x, K)$  in eq. (7). The widths of this region of homogeneity correspond to the space-time variances  $\langle \tilde{x}_\mu \tilde{x}_\nu \rangle(\mathbf{K})$ , see eq.

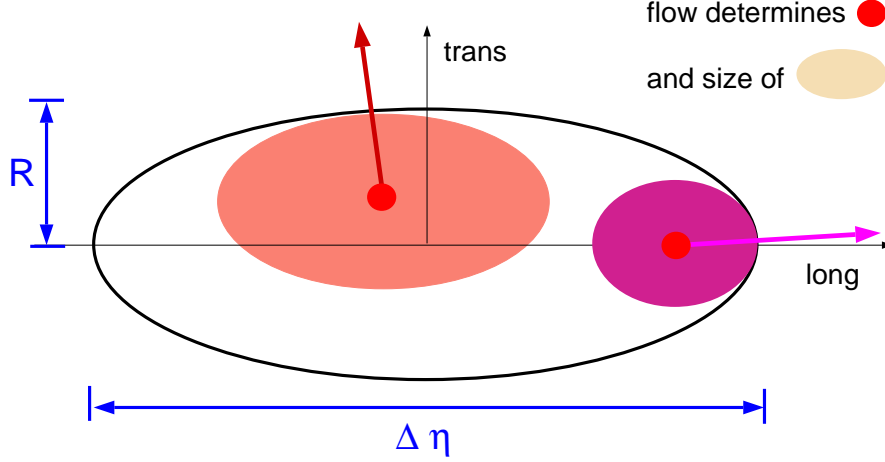


Fig. 2. Sketch of the particle emission region for a collision with collective dynamical expansion. The size and orientation of the average pair momentum  $\mathbf{K}$  serves as wavelength filter: depending on  $\mathbf{K}$  (indicated by arrows), HBT measurements are sensitive to different parts of the collision region.

(10). Thus, HBT radius parameters give access to the space-time variances  $\langle \tilde{x}_\mu \tilde{x}_\nu \rangle(\mathbf{K})$  but they do not depend on the “effective source center”  $\langle x_\mu \rangle$ .

### 2.2.3. The Yano-Koonin-Podgoretskii parametrisation

The Yano-Koonin-Podgoretskii parametrisation eliminates the mass-shell constraint  $K \cdot q = 0$  in (11) by choosing the relative momentum components  $q_\perp = \sqrt{q_o^2 + q_s^2}$ ,  $q^0$  and  $q_l$  as independent. The corresponding Gaussian ansatz reads<sup>102,66,20,36</sup>

$$C(\mathbf{q}, \mathbf{K}) = 1 + \lambda(\mathbf{K}) \exp \left[ -R_\perp^2(\mathbf{K}) q_\perp^2 - R_\parallel^2(\mathbf{K}) (q_l^2 - (q^0)^2) - \left( R_0^2(\mathbf{K}) + R_\parallel^2(\mathbf{K}) \right) (q \cdot U(\mathbf{K}))^2 \right]. \quad (24)$$

Here, the 4-velocity  $U(\mathbf{K})$  has only one  $\mathbf{K}$ -dependent longitudinal spatial component,

$$U(\mathbf{K}) = \frac{1}{\sqrt{1 - v^2(\mathbf{K})}} (1, 0, 0, v(\mathbf{K})) . \quad (25)$$

The combinations of relative momenta  $(q_l^2 - (q^0)^2)$ ,  $(q \cdot U(\mathbf{K}))^2$  and  $q_\perp^2$  appearing in (24) are scalars under longitudinal boosts. Therefore, the three

YKP fit parameters  $R_{\perp}^2(\mathbf{K})$ ,  $R_0^2(\mathbf{K})$ , and  $R_{\parallel}^2(\mathbf{K})$  are longitudinally boost-invariant and do not depend on the longitudinal velocity of the measurement frame. The fourth YKP parameter is the Yano-Koonin (YK) velocity  $v(\mathbf{K})$ . The corresponding rapidity

$$Y_{\text{YK}}(\mathbf{K}) = \frac{1}{2} \ln \left( \frac{1 + v(\mathbf{K})}{1 - v(\mathbf{K})} \right) \quad (26)$$

transforms additively under longitudinal boosts.

Identifying the combinations of relative momenta  $(q_l^2 - (q^0)^2)$ ,  $(q \cdot U(\mathbf{K}))^2$  and  $q_{\perp}^2$  in the Gaussian correlator (11), one can relate the YKP parameters to space-time variances in complete analogy to the Cartesian case. Explicit expressions can be found in the original papers<sup>36,101</sup>. Since the ansatz (24) uses four Gaussian parameters, it provides a complete parametrisation for azimuthally symmetric collisions which is equivalent to the Cartesian Bertsch-Pratt parametrisation. The Gaussian HBT radius parameters of the Cartesian parametrisation can be related to the YKP fit parameters via<sup>36,101</sup>

$$R_s^2 = R_{\perp}^2, \quad (27)$$

$$R_{\text{diff}}^2 = R_o^2 - R_s^2 = \frac{\beta_{\perp}^2}{1 - v^2(\mathbf{K})} \left( R_0^2 + v^2 R_{\parallel}^2 \right), \quad (28)$$

$$R_l^2 = (1 - \beta_l^2) R_{\parallel}^2 + \frac{(\beta_l - v)^2}{1 - v^2(\mathbf{K})} \left( R_0^2 + R_{\parallel}^2 \right), \quad (29)$$

$$R_{ol}^2 = \beta_{\perp} \left( -\beta_l R_{\parallel}^2 + \frac{(\beta_l - v)}{1 - v^2(\mathbf{K})} \left( R_0^2 + R_{\parallel}^2 \right) \right). \quad (30)$$

The space-time interpretation of YKP parameters is studied in detail<sup>36,101,88</sup>. The consistency check (27)-(30) of measured YKP and Cartesian parameters is mandatory for a space-time interpretation of YKP parameters since known technical problems with the YKP parametrization can affect fit parameters significantly<sup>88</sup>.

### 2.3. Collisions at finite impact parameter

#### 2.3.1. Choice of coordinate system

For central collisions, azimuthal symmetry of the collision region allows to use the *osl*-coordinate system which is oriented differently for each particle pair, such that its *out*-axis is parallel to the average pair momentum.

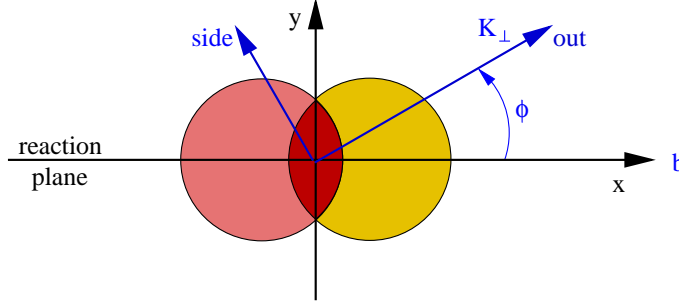


Fig. 3. The impact parameter fixed coordinate system is obtained by rotating the out-side-longitudinal coordinate system by the azimuthal angle  $\Phi = \angle(K_{\perp}, b)$ .

At finite impact parameter, HBT radius parameters  $R_{ij}^2(\mathbf{K})$  depend not only on the modulus of the transverse pair momentum  $|\mathbf{K}|$ , but also on its orientation in the transverse plane which is defined with respect to some pair-independent direction in the laboratory system<sup>92,93,98</sup>. In practice, one introduces the *impact parameter fixed* coordinate system, for which the transverse coordinate  $x$  lies within the reaction plane; the transverse coordinate  $y$  lies orthogonal to it, see Fig. 3. The out-side-longitudinal and the impact parameter fixed system are related by a rotation with respect to the angle  $\Phi = \angle(K_{\perp}, b)$

$$\mathcal{D}_{\Phi} = \begin{pmatrix} \cos \Phi & \sin \Phi & 0 \\ -\sin \Phi & \cos \Phi & 0 \\ 0 & 0 & 1 \end{pmatrix}, \quad (31)$$

such that after rotating to the *osl*-system we have

$$\mathcal{D}_{\Phi} \beta = \begin{pmatrix} \beta_{\perp} \\ 0 \\ \beta_l \end{pmatrix}, \quad \mathcal{D}_{\Phi} \tilde{\mathbf{x}} = \begin{pmatrix} \tilde{x} \cos \Phi + \tilde{y} \sin \Phi \\ -\tilde{x} \sin \Phi + \tilde{y} \cos \Phi \\ \tilde{z} \end{pmatrix}. \quad (32)$$

For non-central collisions, the emission function is written in the impact parameter fixed coordinate system.

### 2.3.2. HBT radius parameters from space-time variances

In eq. (4), the emission function entering the two-particle correlator is written in the *osl*-system. For an emission function in the impact parameter

fixed system, the correlator reads:

$$C(\mathbf{K}, \mathbf{q}) = 1 + |\langle e^{i\mathbf{q} \cdot (\mathcal{D}_\Phi \mathbf{x} - \mathcal{D}_\Phi \beta t)} \rangle|. \quad (33)$$

From this, the HBT radius parameters can be calculated<sup>98</sup>:

$$\begin{aligned} R_{ij}^2(\mathbf{K}) &= - \left. \frac{\partial^2 C(\mathbf{q}, \mathbf{K})}{\partial q_i \partial q_j} \right|_{\mathbf{q}=0} \\ &= \langle [(\mathcal{D}_\Phi \tilde{\mathbf{x}})_i - (\mathcal{D}_\Phi \beta)_i \tilde{t}] [(\mathcal{D}_\Phi \tilde{\mathbf{x}})_j - (\mathcal{D}_\Phi \beta)_j \tilde{t}] \rangle. \end{aligned} \quad (34)$$

As for the azimuthally symmetric case, the HBT radius parameters show implicit and explicit  $K$ -dependences<sup>98</sup>:

$$R_s^2(K_\perp, \Phi, Y) = \langle \tilde{x}^2 \rangle \sin^2 \Phi + \langle \tilde{y}^2 \rangle \cos^2 \Phi - \langle \tilde{x} \tilde{y} \rangle \sin 2\Phi, \quad (35)$$

$$\begin{aligned} R_o^2(K_\perp, \Phi, Y) &= \langle \tilde{x}^2 \rangle \cos^2 \Phi + \langle \tilde{y}^2 \rangle \sin^2 \Phi + \beta_\perp^2 \langle \tilde{t}^2 \rangle \\ &\quad - 2\beta_\perp \langle \tilde{t} \tilde{x} \rangle \cos \Phi - 2\beta_\perp \langle \tilde{t} \tilde{y} \rangle \sin \Phi + \langle \tilde{x} \tilde{y} \rangle \sin 2\Phi, \end{aligned} \quad (36)$$

$$\begin{aligned} R_{os}^2(K_\perp, \Phi, Y) &= \langle \tilde{x} \tilde{y} \rangle \cos 2\Phi + \frac{1}{2} \sin 2\Phi (\langle \tilde{y}^2 \rangle - \langle \tilde{x}^2 \rangle) \\ &\quad + \beta_\perp \langle \tilde{t} \tilde{x} \rangle \sin \Phi - \beta_\perp \langle \tilde{t} \tilde{y} \rangle \cos \Phi, \end{aligned} \quad (37)$$

$$R_t^2(K_\perp, \Phi, Y) = \langle (\tilde{z} - \beta_t \tilde{t})^2 \rangle, \quad (38)$$

$$R_{ol}^2(K_\perp, \Phi, Y) = \langle (\tilde{z} - \beta_t \tilde{t})(\tilde{x} \cos \Phi + \tilde{y} \sin \Phi - \beta_\perp \tilde{t}) \rangle, \quad (39)$$

$$R_{sl}^2(K_\perp, \Phi, Y) = \langle (\tilde{z} - \beta_t \tilde{t})(\tilde{y} \cos \Phi - \tilde{x} \sin \Phi) \rangle. \quad (40)$$

On the r.h.s. of these equations we only displayed the *explicit*  $\Phi$ -dependences which are a geometrical consequence of rotating the *out*-axis from the direction of the impact parameter  $\mathbf{b}$  to the direction of the average pair momentum  $\mathbf{K}_\perp$ . The *implicit*  $\Phi$ -dependence of the space-time variances,

$$\langle \tilde{x}_\mu \tilde{x}_\nu \rangle = \langle \tilde{x}_\mu \tilde{x}_\nu \rangle(K_\perp, \Phi, Y), \quad (41)$$

characterises the dynamical correlations between the size of the effective emission region and the azimuthal direction in which particles are emitted. The role of explicit and implicit contributions is illustrated in Fig. 4.

### 2.3.3. Symmetries satisfied by space-time variances

The implicit  $\Phi$ -dependence of space-time variances can be characterised in terms of the Fourier coefficients  $\langle \dots \rangle_n^c$  and  $\langle \dots \rangle_n^s$

$$\langle \tilde{x}_\mu \tilde{x}_\nu \rangle(\Phi) = \sum_{n=0}^{\infty} \langle \tilde{x}_\mu \tilde{x}_\nu \rangle_n^c \cos(n\Phi) + \langle \tilde{x}_\mu \tilde{x}_\nu \rangle_n^s \sin(n\Phi). \quad (42)$$

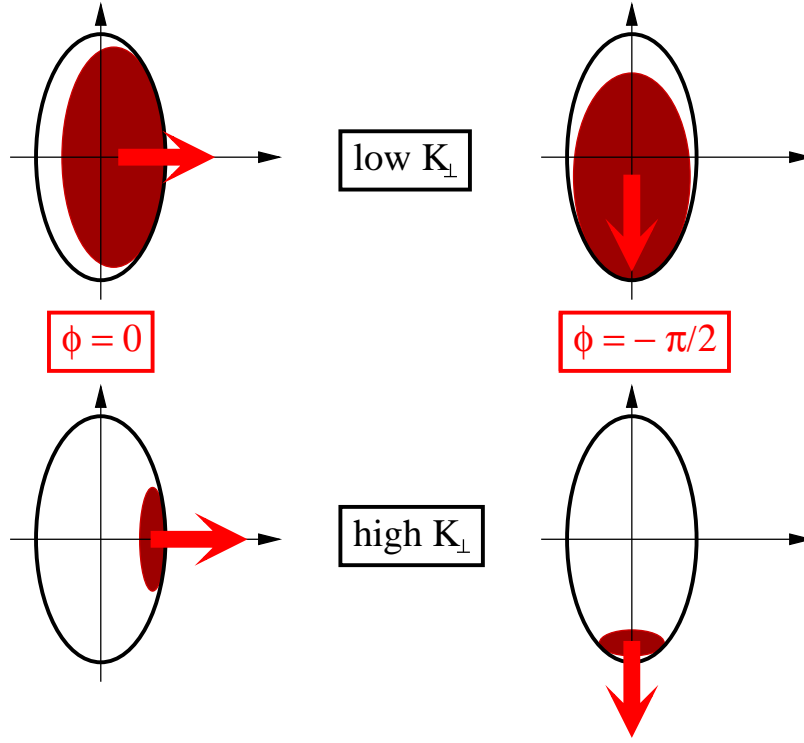


Fig. 4. Schematic picture of the role of explicit and implicit  $\phi$ -dependence in the transverse plane. At small transverse pair momentum, the orientation of the region of homogeneity follows the global geometry, and the explicit  $\Phi$ -dependence is expected to dominate. At large transverse pair momentum, the orientation and shape of the region of homogeneity can deviate significantly from the global geometry. In this case, the implicit  $\Phi$ -dependence of HBT radius parameters becomes significant, see text.

Several symmetries allow to constrain this most general implicit  $\Phi$ -dependence<sup>98,57,39</sup>:

(1) Mirror symmetry with respect to the reaction plane:

This symmetry of the emission function holds at both mid and forward rapidity. It implies that space-time variances linear in  $\tilde{y}$  change sign under  $\Phi \rightarrow -\Phi$ , while space-time variances which are not linear in  $\tilde{y}$

are invariant under the mirror symmetry,

$$\langle \tilde{x}_\mu \tilde{x}_\nu \rangle(\Phi) = -\langle \tilde{x}_\mu \tilde{x}_\nu \rangle(-\Phi), \quad \text{for either } \tilde{x}_\mu = \tilde{y} \text{ or } \tilde{x}_\nu = \tilde{y}, \quad (43)$$

$$\langle \tilde{x}_\mu \tilde{x}_\nu \rangle(\Phi) = \langle \tilde{x}_\mu \tilde{x}_\nu \rangle(-\Phi), \quad \text{for } \tilde{x}_\mu, \tilde{x}_\nu \neq \tilde{y}, \quad (44)$$

$$\langle \tilde{y}^2 \rangle(\Phi) = \langle \tilde{y}^2 \rangle(-\Phi). \quad (45)$$

(2) Point symmetry at mid-rapidity:

For collisions between equal mass nuclei, the total emission region is point symmetric under  $(\tilde{x}, \tilde{y}, \tilde{z}) \rightarrow (-\tilde{x}, -\tilde{y}, -\tilde{z})$  at mid-rapidity. This is a symmetry under  $\Phi \rightarrow \Phi + \pi$ . At mid-rapidity, we thus have the additional requirement

$$\langle \tilde{x}_\mu \tilde{x}_\nu \rangle(\Phi) = -\langle \tilde{x}_\mu \tilde{x}_\nu \rangle(\Phi + \pi), \quad \text{for either } \tilde{x}_\mu = \tilde{t} \text{ or } \tilde{x}_\nu = \tilde{t}, \quad (46)$$

$$\langle \tilde{x}_\mu \tilde{x}_\nu \rangle(\Phi) = \langle \tilde{x}_\mu \tilde{x}_\nu \rangle(\Phi + \pi), \quad \text{for } \tilde{x}_\mu, \tilde{x}_\nu \neq \tilde{t}, \quad (47)$$

$$\langle \tilde{t}^2 \rangle(\Phi) = \langle \tilde{t}^2 \rangle(\Phi + \pi). \quad (48)$$

At forward rapidity, this point symmetry does not constrain the azimuthal dependence since the same symmetry maps  $K_l \rightarrow -K_l$  on which the space-time variances depend implicitly.

Both symmetries imply that many of the Fourier coefficients vanish in the harmonic expansion (42) of the space-time variances. A complete overview is given in Table 1. We discuss now the implications of these symmetries for a harmonic analysis of HBT radius parameters whose  $\Phi$ -dependences are characterised in terms of harmonic coefficients

$$R_{ij,m}^c{}^2 = \frac{1}{2\pi} \int_{-\pi}^{\pi} R_{ij}^2 \cos(m\Phi) d\Phi, \quad (49)$$

$$R_{ij,m}^s{}^2 = \frac{1}{2\pi} \int_{-\pi}^{\pi} R_{ij}^2 \sin(m\Phi) d\Phi. \quad (50)$$

#### 2.3.4. Explicit azimuthal dependences at mid-rapidity

As long as  $\Phi$ -dependent position-momentum correlations in the source are weak compared to the global essentially geometrical asymmetry of the finite impact parameter collision, the implicit  $\Phi$ -dependence can be neglected compared to the explicit one. In this case, all space-time variances (42) are characterised by their zeroth Fourier components. Inserting the zeroth components listed in Table 1 into the expressions for the HBT radius parameters



Table 1. Space-time variances for central and non-central collisions

$\langle x_\mu x_\nu \rangle$	$\mathbf{b} = 0$ $K_\perp \neq 0$	$\mathbf{b} = 0$ $K_\perp = 0$	$\mathbf{b} \neq 0$ $Y = 0$ $n = 0$	$\mathbf{b} \neq 0$ $Y \neq 0$ $n = 0$	$\mathbf{b} \neq 0$ $Y = 0$ $n \text{ even}$	$\mathbf{b} \neq 0$ $Y = 0$ $n \text{ odd}$	$\mathbf{b} \neq 0$ $Y \neq 0$ $n \geq 1$	
$\langle \tilde{x} \tilde{x} \rangle$	$\times$	$\times$	$\times$	$\times$	$\times$ 0	0 0	$\times$ 0	cos sin
$\langle \tilde{x} \tilde{y} \rangle$	0	0	0	0	0 $\times$	0 0	0 $\times$	cos sin
$\langle \tilde{y} \tilde{y} \rangle$	$\times$	$\times$	$\times$	$\times$	$\times$ 0	0 0	$\times$ 0	cos sin
$\langle \tilde{x} \tilde{z} \rangle$	$\times$	0	$\times$	$\times$	$\times$ 0	0 0	$\times$ 0	cos sin
$\langle \tilde{y} \tilde{z} \rangle$	0	0	0	0	0 $\times$	0 0	0 $\times$	cos sin
$\langle \tilde{z} \tilde{z} \rangle$	$\times$	$\times$	$\times$	$\times$	$\times$ 0	0 0	$\times$ 0	cos sin
$\langle \tilde{x} \tilde{t} \rangle$	$\times$	0	0	$\times$	0 0	$\times$ 0	$\times$ 0	cos sin
$\langle \tilde{y} \tilde{t} \rangle$	0	0	0	0	0 0	0 $\times$	0 $\times$	cos sin
$\langle \tilde{z} \tilde{t} \rangle$	$\times$	$\times$	0	$\times$	0 0	$\times$ 0	$\times$ 0	cos sin
$\langle \tilde{t} \tilde{t} \rangle$	$\times$	$\times$	$\times$	$\times$	$\times$ 0	0 0	$\times$ 0	cos sin

The non-vanishing ( $\times$ ) and vanishing (0) space-time variances for central ( $\mathbf{b} = 0$ ) and non-central ( $\mathbf{b} \neq 0$ ) collision systems at mid-rapidity ( $Y = 0$ ) and away from mid-rapidity. For non-central collisions, the harmonic coefficients  $\langle \dots \rangle_n^c$  and  $\langle \dots \rangle_n^s$  are listed in the three rightmost columns. Away from mid-rapidity, no symmetry ensures a different behaviour of odd and even harmonics.

(35)–(40), one finds<sup>98,57</sup>:

$$R_s^2(K_\perp, \Phi, Y) = \frac{1}{2} (\langle \tilde{x}^2 \rangle + \langle \tilde{y}^2 \rangle) + \frac{1}{2} (\langle \tilde{y}^2 \rangle - \langle \tilde{x}^2 \rangle) \cos 2\Phi, \quad (51)$$

$$R_o^2(K_\perp, \Phi, Y) = \frac{1}{2} (\langle \tilde{x}^2 \rangle + \langle \tilde{y}^2 \rangle) - \frac{1}{2} (\langle \tilde{y}^2 \rangle - \langle \tilde{x}^2 \rangle) \cos 2\Phi + \beta_\perp^2 \langle \tilde{t}^2 \rangle, \quad (52)$$

$$R_{os}^2(K_\perp, \Phi, Y) = \frac{1}{2} (\langle \tilde{y}^2 \rangle - \langle \tilde{x}^2 \rangle) \sin 2\Phi, \quad (53)$$

$$R_l^2(K_\perp, \Phi, Y) = \langle \tilde{z}^2 \rangle + \beta_l^2 \langle \tilde{t}^2 \rangle, \quad (54)$$

$$R_{ol}^2(K_\perp, \Phi, Y) = \langle \tilde{x} \tilde{z} \rangle \cos \Phi, \quad (55)$$

$$R_{sl}^2(K_\perp, \Phi, Y) = -\langle \tilde{x} \tilde{z} \rangle \sin \Phi. \quad (56)$$

Two  $\Phi$ -dependent geometrical informations are contained in these equations:

(1) Eccentricity of the emission ellipsoid in the transverse plane<sup>98</sup>

The HBT radius parameters  $R_o^2$ ,  $R_s^2$  and  $R_{os}^2$  are sensitive to the extension of the emission region in the transverse plane. They show second harmonic oscillations of the same strength  $\frac{1}{2}(\langle \tilde{x}^2 \rangle - \langle \tilde{y}^2 \rangle)$  and thus measure the eccentricity of the emission ellipsoid in the transverse plane. The second harmonic coefficients of HBT radius parameters thus satisfy the rules

$$R_{o,2}^{s\,2} = 0, \quad R_{s,2}^{s\,2} = 0, \quad R_{os,2}^{c\,2} = 0, \quad (57)$$

$$R_{o,2}^{c\,2} = -R_{s,2}^{c\,2} = -R_{os,2}^{s\,2}. \quad (58)$$

While (57) must be always satisfied at mid-rapidity because of the symmetry requirements (see also next section), deviations from (58) are an unambiguous sign for implicit  $\Phi$ -dependences of space-time variances, i.e. for azimuthally dependent position-momentum correlations in the source.

(2) Tilt of the emission ellipsoid in the reaction plane<sup>57</sup>

The HBT radius parameters  $R_{ol}^2$  and  $R_{sl}^2$  are sensitive to the off-diagonal component  $\langle \tilde{x}\tilde{z} \rangle$ . They measure the angle  $\Theta$  by which the major longitudinal axis of the emission ellipsoid is tilted away from the beam direction, see Fig. 5,

$$\Theta = \frac{1}{2} \tan^{-1} \left( \frac{2\langle \tilde{x}\tilde{z} \rangle}{\langle \tilde{z}\tilde{z} \rangle - \langle \tilde{x}\tilde{x} \rangle} \right). \quad (59)$$

The tilt  $\Theta$  is measured from the first harmonic oscillations at mid-rapidity. Any deviation from the rule

$$R_{ol,1}^{c\,2} = -R_{sl,1}^{s\,2}. \quad (60)$$

is an unambiguous sign for strong azimuthally dependent position-momentum correlations in the source. Again, symmetry constraints generally require

$$R_{ol,1}^{s\,2} = 0, \quad (61)$$

$$R_{sl,1}^{c\,2} = 0. \quad (62)$$

2.3.5. *Implicit azimuthal dependence at mid-rapidity*

To access the effect of an implicit  $\Phi$ -dependence of space-time variances, we expand the radius parameters (35)–(40) in power of the harmonic

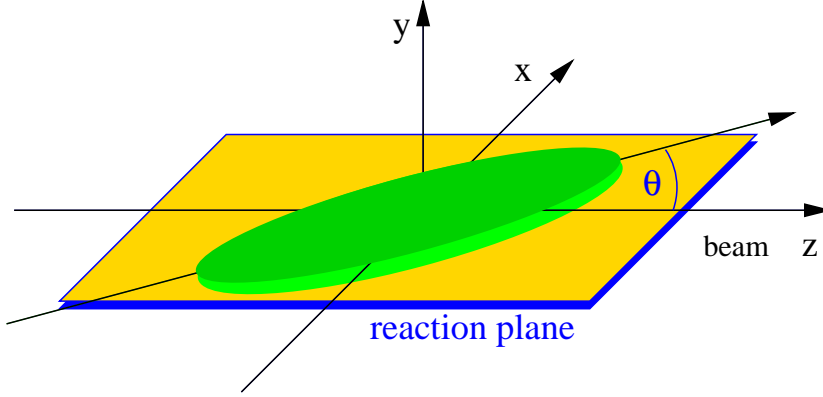


Fig. 5. In general, the main axis of the emission ellipsoid is tilted for finite impact parameter collisions by an angle  $\Theta$  with respect to the beam axis. This tilt can be measured via the first harmonics of the off-diagonal HBT radius parameters  $R_{ol}^2$  and  $R_{sl}^2$  at mid-rapidity.

coefficients<sup>98,39</sup>. The following discussion includes all harmonic contributions allowed by the symmetries. It may simplify further if the emission function is sufficiently smoothly shaped for higher harmonic coefficients to be negligible,

$$\langle \tilde{x}_\mu \tilde{x}_\nu \rangle_n^{s/c} \gg \langle \tilde{x}_\mu \tilde{x}_\nu \rangle_{2+n}^{s/c}. \quad (63)$$

Using the Fourier expansion (42) of space-time variances at mid-rapidity, one finds:

1. The zeroth moments of the HBT radius parameters:

$$R_{s,0}^2 = \frac{1}{2} (\langle \tilde{x}^2 \rangle_0 + \langle \tilde{y}^2 \rangle_0) + \frac{1}{4} \langle \tilde{y}^2 \rangle_2^c - \frac{1}{2} \langle \tilde{x} \tilde{y} \rangle_2^s - \frac{1}{4} \langle \tilde{x}^2 \rangle_2^c, \quad (64)$$

$$R_{o,0}^2 = \frac{1}{2} (\langle \tilde{x}^2 \rangle_0 + \langle \tilde{y}^2 \rangle_0) + \beta_\perp^2 \langle \tilde{t}^2 \rangle_0 + \frac{1}{4} \langle \tilde{x}^2 \rangle_2^c + \frac{1}{2} \langle \tilde{x} \tilde{y} \rangle_2^s - \frac{1}{4} \langle \tilde{y}^2 \rangle_2^c - \beta_\perp (\langle \tilde{x} \tilde{t} \rangle_1^c + \langle \tilde{y} \tilde{t} \rangle_1^s), \quad (65)$$

$$R_{l,0}^2 = \langle \tilde{z}^2 \rangle_0. \quad (66)$$

These expressions show that contributions to the absolute size of azimuthally averaged HBT radius parameters stem not only from the azimuthal averages  $\langle \tilde{x}_\mu \tilde{x}_\nu \rangle_0$ , but also from the harmonic oscillations of these space-time variances. Nevertheless, only those Fourier components of the

HBT radius parameters are non-zero, which were found to be non-zero in the case without implicit  $\Phi$ -dependence. This continues to be the case for 2. The first moments of the HBT radius parameters:

The only non-vanishing first moments are

$$R_{ol,1}^c{}^2 = \langle \tilde{x}\tilde{z} \rangle_0 + \frac{1}{2} (\langle \tilde{x}\tilde{z} \rangle_2^c + \langle \tilde{y}\tilde{z} \rangle_2^s) - \beta_\perp \langle \tilde{z}\tilde{t} \rangle_1^c, \quad (67)$$

$$R_{sl,1}^c{}^2 = -\langle \tilde{x}\tilde{z} \rangle_0 + \frac{1}{2} (\langle \tilde{x}\tilde{z} \rangle_2^c + \langle \tilde{y}\tilde{z} \rangle_2^s). \quad (68)$$

For the case of a static source, these quantities determine the tilt angle (59) and satisfy  $R_{ol,1}^c{}^2 = -R_{sl,1}^s{}^2$ . According to eqs. (67) and (68), a non-zero value of

$$R_{ol,1}^c{}^2 + R_{sl,1}^c{}^2 = \langle \tilde{x}\tilde{z} \rangle_2^c + \langle \tilde{y}\tilde{z} \rangle_2^s - \beta_\perp \langle \tilde{z}\tilde{t} \rangle_1^c \quad (69)$$

is an unambiguous sign of dynamically generated  $\Phi$ -dependent correlations in the source.

3. The second moments of the HBT radius parameters:

The only non-vanishing second moments are

$$R_{s,2}^c{}^2 = \frac{1}{2} (\langle \tilde{y}^2 \rangle_0 - \langle \tilde{x}^2 \rangle_0) + \frac{1}{2} (\langle \tilde{y}^2 \rangle_2^c + \langle \tilde{x}^2 \rangle_2^c) - \frac{1}{4} (\langle \tilde{x}^2 \rangle_4^c - \langle \tilde{y}^2 \rangle_4^c) - \frac{1}{2} \langle \tilde{x}\tilde{y} \rangle_4^s, \quad (70)$$

$$R_{o,2}^c{}^2 = -\frac{1}{2} (\langle \tilde{y}^2 \rangle_0 - \langle \tilde{x}^2 \rangle_0) + \frac{1}{2} (\langle \tilde{y}^2 \rangle_2^c + \langle \tilde{x}^2 \rangle_2^c) - \beta_\perp (\langle \tilde{x}\tilde{t} \rangle_1^c - \langle \tilde{y}\tilde{t} \rangle_1^s) + \beta_\perp^2 \langle \tilde{t}^2 \rangle_2^c - \beta_\perp (\langle \tilde{x}\tilde{t} \rangle_3^c + \langle \tilde{y}\tilde{t} \rangle_3^s) + \frac{1}{4} (\langle \tilde{x}^2 \rangle_4^c - \langle \tilde{y}^2 \rangle_4^c) + \frac{1}{2} \langle \tilde{x}\tilde{y} \rangle_4^s, \quad (71)$$

$$R_{os,2}^s{}^2 = \frac{1}{2} (\langle \tilde{y}^2 \rangle_0 - \langle \tilde{x}^2 \rangle_0) + \frac{\beta_\perp}{2} (\langle \tilde{x}\tilde{t} \rangle_1^c - \langle \tilde{y}\tilde{t} \rangle_1^s) - \frac{\beta_\perp}{2} (\langle \tilde{x}\tilde{t} \rangle_3^c + \langle \tilde{y}\tilde{t} \rangle_3^s) - \frac{1}{4} (\langle \tilde{x}^2 \rangle_4^c - \langle \tilde{y}^2 \rangle_4^c) + \frac{1}{2} \langle \tilde{x}\tilde{y} \rangle_4^s, \quad (72)$$

$$R_{l,2}^c{}^2 = \langle \tilde{z}^2 \rangle_2^c. \quad (73)$$

The equations (57) remain true in the presence of  $\Phi$ -dependent position-momentum gradients in the source, while deviations from the  $R_{o,2}^c{}^2 = -R_{s,2}^c{}^2 = -R_{os,2}^s{}^2$  rule (58) are an unambiguous sign for an implicit  $\Phi$ -

dependence, namely:

$$R_{o,2}^{c\,2} + R_{s,2}^{c\,2} = \langle \tilde{x}^2 \rangle_2^c + \langle \tilde{y}^2 \rangle_2^c + \beta_\perp^2 \langle \tilde{t}^2 \rangle_2^c - \beta_\perp (\langle \tilde{x}\tilde{t} \rangle_1^c - \langle \tilde{y}\tilde{t} \rangle_1^s + \langle \tilde{x}\tilde{t} \rangle_3^c + \langle \tilde{y}\tilde{t} \rangle_3^s), \quad (74)$$

$$R_{o,2}^{c\,2} + R_{os,2}^{s\,2} = \frac{1}{2} (\langle \tilde{x}^2 \rangle_2^c + \langle \tilde{y}^2 \rangle_2^c) + \beta_\perp^2 \langle \tilde{t}^2 \rangle_2^c - \frac{\beta_\perp}{2} (\langle \tilde{x}\tilde{t} \rangle_1^c - \langle \tilde{y}\tilde{t} \rangle_1^s) + \langle \tilde{x}\tilde{y} \rangle_4^s - \frac{3}{2} \beta_\perp (\langle \tilde{x}\tilde{t} \rangle_3^c + \langle \tilde{y}\tilde{t} \rangle_3^s) + \frac{1}{2} (\langle \tilde{x}^2 \rangle_4^c - \langle \tilde{y}^2 \rangle_4^c), \quad (75)$$

$$R_{s,2}^{c\,2} - R_{os,2}^{s\,2} = \frac{1}{2} (\langle \tilde{x}^2 \rangle_2^c + \langle \tilde{y}^2 \rangle_2^c) - \frac{1}{2} \beta_\perp (\langle \tilde{x}\tilde{t} \rangle_1^c - \langle \tilde{y}\tilde{t} \rangle_1^s - \langle \tilde{x}\tilde{t} \rangle_3^c - \langle \tilde{y}\tilde{t} \rangle_3^s) - \frac{1}{2} (\langle \tilde{x}^2 \rangle_4^c - \langle \tilde{y}^2 \rangle_4^c) - \langle \tilde{x}\tilde{y} \rangle_4^s. \quad (76)$$

If the fourth order moments  $\langle \tilde{x}^2 \rangle_4^c - \langle \tilde{y}^2 \rangle_4^c$  and  $\langle \tilde{x}\tilde{y} \rangle_4^s$  are negligible and if the transverse pair momentum  $K_\perp$  is sufficiently small, then

$$R_{s,2}^{c\,2} - R_{os,2}^{s\,2} \approx R_{o,2}^{c\,2} + R_{os,2}^{s\,2}. \quad (77)$$

#### 4. The $n$ -th moments of the HBT radius parameters ( $n > 2$ ):

In general, the properties of the sin and cos functions imply that the  $n$ -th order harmonics  $R_{ij,n}^{s\,2}$ ,  $R_{ij,n}^{c\,2}$  in eqs. (49), (50) are built up of  $m$ -th order harmonics  $\langle \tilde{x}_\mu \tilde{y}_\nu \rangle_m^s$ ,  $\langle \tilde{x}_\mu \tilde{y}_\nu \rangle_m^c$  with  $n-2 \leq m \leq n+2$ . This limits the number of terms appearing in  $n$ -th order expressions. Since it is an open question whether the approximation (63) applies for realistic sources<sup>b</sup>, we give these expressions here for completeness.

For the *side-long* and *out-long* HBT radius parameters, only odd harmonic terms appear. For  $n = 3, 5, 7, \dots$ , we have

$$R_{ol,n}^{c\,2} = \frac{1}{2} (\langle \tilde{x}\tilde{z} \rangle_{n-1}^c - \langle \tilde{y}\tilde{z} \rangle_{n-1}^s) - \beta_\perp \langle \tilde{z}\tilde{t} \rangle_n^c + \frac{1}{2} (\langle \tilde{x}\tilde{z} \rangle_{n+1}^c + \langle \tilde{y}\tilde{z} \rangle_{n+1}^s), \quad (78)$$

$$R_{sl,n}^{s\,2} = \frac{1}{2} (\langle \tilde{y}\tilde{z} \rangle_{n-1}^s - \langle \tilde{x}\tilde{z} \rangle_{n-1}^c) + \frac{1}{2} (\langle \tilde{y}\tilde{z} \rangle_{n+1}^s + \langle \tilde{x}\tilde{z} \rangle_{n+1}^c). \quad (79)$$

The Fourier decomposition of the other HBT radius parameters contains

---

<sup>b</sup>We thank Mike Lisa for drawing our attention to this issue.

only even harmonic terms. For  $n = 4, 6, 8, \dots$ , we have

$$\begin{aligned} R_{s,n}^{c\ 2} = & -\frac{1}{4} \left( \langle \tilde{x}^2 \rangle_{n-2}^c - \langle \tilde{y}^2 \rangle_{n-2}^c \right) + \frac{1}{2} \langle \tilde{x}\tilde{y} \rangle_{n-2}^s \\ & + \frac{1}{2} \left( \langle \tilde{x}^2 \rangle_n^c + \langle \tilde{y}^2 \rangle_n^c \right) \\ & - \frac{1}{4} \left( \langle \tilde{x}^2 \rangle_{n+2}^c - \langle \tilde{y}^2 \rangle_{n+2}^c \right) - \frac{1}{2} \langle \tilde{x}\tilde{y} \rangle_{n+2}^s, \end{aligned} \quad (80)$$

$$\begin{aligned} R_{o,n}^{c\ 2} = & \frac{1}{4} \left( \langle \tilde{x}^2 \rangle_{n-2}^c - \langle \tilde{y}^2 \rangle_{n-2}^c \right) - \frac{1}{2} \langle \tilde{x}\tilde{y} \rangle_{n-2}^s \\ & - \beta_{\perp} \left( \langle \tilde{x}\tilde{t} \rangle_{n-1}^c - \langle \tilde{y}\tilde{t} \rangle_{n-1}^s \right) \\ & + \frac{1}{2} \left( \langle \tilde{x}^2 \rangle_n^c + \langle \tilde{y}^2 \rangle_n^c \right) + \beta_{\perp}^2 \langle \tilde{t}^2 \rangle_n^c \\ & - \beta_{\perp} \left( \langle \tilde{x}\tilde{t} \rangle_{n+1}^c + \langle \tilde{y}\tilde{t} \rangle_{n+1}^s \right) \\ & + \frac{1}{4} \left( \langle \tilde{x}^2 \rangle_{n+2}^c - \langle \tilde{y}^2 \rangle_{n+2}^c \right) + \frac{1}{2} \langle \tilde{x}\tilde{y} \rangle_{n+2}^s, \end{aligned} \quad (81)$$

$$\begin{aligned} R_{os,n}^{s\ 2} = & -\frac{1}{4} \left( \langle \tilde{x}^2 \rangle_{n-2}^c - \langle \tilde{y}^2 \rangle_{n-2}^c \right) + \frac{1}{2} \langle \tilde{x}\tilde{y} \rangle_{n-2}^s \\ & + \frac{1}{2} \beta_{\perp} \left( \langle \tilde{x}\tilde{t} \rangle_{n-1}^c - \langle \tilde{y}\tilde{t} \rangle_{n-1}^s \right) \\ & - \frac{1}{2} \beta_{\perp} \left( \langle \tilde{x}\tilde{t} \rangle_{n+1}^c + \langle \tilde{y}\tilde{t} \rangle_{n+1}^s \right) \\ & - \frac{1}{4} \left( \langle \tilde{x}^2 \rangle_{n+2}^c - \langle \tilde{y}^2 \rangle_{n+2}^c \right) + \frac{1}{2} \langle \tilde{x}\tilde{y} \rangle_{n+2}^s, \end{aligned} \quad (82)$$

$$R_{l,n}^{c\ 2} = \langle \tilde{z}^2 \rangle_n^c. \quad (83)$$

Whether these higher harmonic coefficients are numerically important remains to be established experimentally.

### 2.3.6. Implicit azimuthal dependence at forward rapidity

At non-central rapidity  $Y \neq 0$ , additional Fourier components of the space-time variances can contribute to HBT radius parameters, as is seen from Table 1. The reason is that at  $Y \neq 0$ , the symmetries (46)–(48) do not hold. It is remarkable that the zeroth and second moments of the out, side and out-side radius parameters, given in eqs. (64), (65), (70), (71) and (72), do not receive extra contributions at forward rapidity. In particular, this implies that deviations from the  $R_{o,2}^{c\ 2} = -R_{s,2}^{c\ 2} = R_{os,2}^{s\ 2}$  rule of (58) remains an unambiguous test for the presence of angular dependent

position-momentum correlations at all rapidities. In addition, the out, side and out-side radius parameters acquire first harmonic oscillations away from mid-rapidity,

$$R_{s,1}^c{}^2 = \frac{1}{4} (\langle \tilde{x}^2 \rangle_1^c - 2\langle \tilde{x}\tilde{y} \rangle_1^s + 3\langle \tilde{y}^2 \rangle_1^c) - \frac{1}{4} (\langle \tilde{x}^2 \rangle_3^c + 2\langle \tilde{x}\tilde{y} \rangle_3^s - \langle \tilde{y}^2 \rangle_3^c), \quad (84)$$

$$R_{o,1}^c{}^2 = \frac{1}{4} (3\langle \tilde{x}^2 \rangle_1^c + 2\langle \tilde{x}\tilde{y} \rangle_1^s + \langle \tilde{y}^2 \rangle_1^c) - \beta_\perp (2\langle \tilde{x}\tilde{t} \rangle_0 + \langle \tilde{x}\tilde{t} \rangle_2^c + \langle \tilde{y}\tilde{t} \rangle_2^c) + \beta_\perp^2 \langle \tilde{t}^2 \rangle_1^c + \frac{1}{4} (\langle \tilde{x}^2 \rangle_3^c + 2\langle \tilde{x}\tilde{y} \rangle_3^s - \langle \tilde{y}^2 \rangle_3^c), \quad (85)$$

$$R_{os,1}^s{}^2 = \frac{1}{4} (-\langle \tilde{x}^2 \rangle_1^c - 2\langle \tilde{x}\tilde{y} \rangle_1^s + \langle \tilde{y}^2 \rangle_1^c) + \beta_\perp \langle \tilde{x}\tilde{t} \rangle_0 - \frac{1}{2}\beta_\perp (\langle \tilde{x}\tilde{t} \rangle_2^c + \langle \tilde{y}\tilde{t} \rangle_2^c) + \frac{1}{4} (\langle \tilde{x}^2 \rangle_3^c + 2\langle \tilde{x}\tilde{y} \rangle_3^s - \langle \tilde{y}^2 \rangle_3^c). \quad (86)$$

In the so-called blast wave model<sup>153</sup>, there is no correlation between the transverse position and the time at which particles are emitted. Hence, the space-time variances linear in  $\tilde{t}$  vanish. Also, the emission duration  $\langle \tilde{t}^2 \rangle$  does not depend on the azimuthal angle. In addition, if the source shows a sufficiently smooth azimuthal dependence for the third order terms  $\langle \tilde{x}^2 \rangle_3^c$ ,  $\langle \tilde{x}\tilde{y} \rangle_3^s$ ,  $\langle \tilde{y}^2 \rangle_3^c$  to be negligible, then

$$R_{s,1}^c{}^2 - R_{o,1}^c{}^2 \approx 2R_{os,1}^s{}^2. \quad (87)$$

Moreover, it was observed in a class of model studies<sup>98</sup> that  $\langle \tilde{x}^2 \rangle_1^c$  should be much larger than  $\langle \tilde{x}\tilde{y} \rangle_1^s$  and  $\langle \tilde{y}^2 \rangle_1^c$ , since asymmetries with respect to the beam axis will occur predominantly in the direction of the impact parameter. This translates into the rule

$$R_{o,1}^c{}^2 : R_{s,1}^c{}^2 : R_{os,1}^s{}^2 = 3 : 1 : -1. \quad (88)$$

A test of (87), (88) allows to establish whether these additional model-dependent assumptions are satisfied.

The three HBT radius parameters  $R_l^2$ ,  $R_{ol}^2$  and  $R_{sl}^2$  involve longitudinal information and depend on the longitudinal velocity  $\beta_l$ . This leads to additional contributions away from mid-rapidity. For completeness, we list here

the non-vanishing first and second moments:

$$R_{l,1}^c{}^2 = \langle \tilde{z}^2 \rangle_1^c - 2\beta_l \langle \tilde{z}\tilde{t} \rangle_1^c + \beta_l^2 \langle \tilde{t}^2 \rangle_1^c, \quad (89)$$

$$R_{l,2}^c{}^2 = \langle \tilde{z}^2 \rangle_2^c - 2\beta_l \langle \tilde{z}\tilde{t} \rangle_2^c + \beta_l^2 \langle \tilde{t}^2 \rangle_2^c, \quad (90)$$

$$\begin{aligned} R_{ol,1}^c{}^2 &= \langle \tilde{x}\tilde{z} \rangle_0 + \frac{1}{2} (\langle \tilde{x}\tilde{z} \rangle_2^c + \langle \tilde{y}\tilde{z} \rangle_2^s) - \beta_\perp \langle \tilde{z}\tilde{t} \rangle_1^c \\ &\quad + \frac{1}{2} \beta_l (2\beta_\perp \langle \tilde{t}^2 \rangle_1^c - 2\langle \tilde{x}\tilde{t} \rangle_0 - \langle \tilde{x}\tilde{t} \rangle_2^c - \langle \tilde{y}\tilde{t} \rangle_2^s), \end{aligned} \quad (91)$$

$$\begin{aligned} R_{ol,2}^c{}^2 &= \frac{1}{2} (\langle \tilde{x}\tilde{z} \rangle_1^c - \langle \tilde{y}\tilde{z} \rangle_1^s) - \beta_\perp \langle \tilde{z}\tilde{t} \rangle_2^c \\ &\quad + \frac{1}{2} \beta_l (2\beta_\perp \langle \tilde{t}^2 \rangle_2^c - \langle \tilde{x}\tilde{t} \rangle_1^c + \langle \tilde{y}\tilde{t} \rangle_1^s) \\ &\quad + \frac{1}{2} (\langle \tilde{x}\tilde{z} \rangle_3^c + \langle \tilde{y}\tilde{z} \rangle_3^s) - \frac{\beta_l}{3} (\langle \tilde{x}\tilde{t} \rangle_3^c + \langle \tilde{y}\tilde{t} \rangle_3^s), \end{aligned} \quad (92)$$

$$\begin{aligned} R_{sl,1}^s{}^2 &= -\langle \tilde{x}\tilde{z} \rangle_0 + \frac{1}{2} (\langle \tilde{x}\tilde{z} \rangle_2^c + \langle \tilde{y}\tilde{z} \rangle_2^s) \\ &\quad + \frac{1}{2} \beta_l (2\langle \tilde{x}\tilde{t} \rangle_0 - \langle \tilde{x}\tilde{t} \rangle_2^c - \langle \tilde{y}\tilde{t} \rangle_2^s), \end{aligned} \quad (93)$$

$$\begin{aligned} R_{sl,2}^s{}^2 &= \frac{1}{2} (\langle \tilde{y}\tilde{z} \rangle_1^s - \langle \tilde{x}\tilde{z} \rangle_1^c) + \frac{1}{2} \beta_l (\langle \tilde{x}\tilde{t} \rangle_1^c - \langle \tilde{y}\tilde{t} \rangle_1^s) \\ &\quad + \frac{1}{2} (\langle \tilde{x}\tilde{z} \rangle_3^c + \langle \tilde{y}\tilde{z} \rangle_3^s) - \frac{\beta_l}{2} (\langle \tilde{x}\tilde{t} \rangle_3^c + \langle \tilde{y}\tilde{t} \rangle_3^s). \end{aligned} \quad (94)$$

### 2.3.7. Reconstruction of the reaction plane

The above analysis of HBT radius parameters for non-central collisions requires the measurement of the angle  $\Phi$  and thus assumes knowledge about the event-wise orientation of the reaction plane. This orientation  $\Psi_R$  is usually measured from the azimuthal dependence of single-particle transverse momentum spectra<sup>63,65</sup>

$$\begin{aligned} E \frac{dN}{d^3p} &= \frac{d^3N}{p_t dp_t dy d\phi} = \int d^4x S(x, p) \\ &= \frac{1}{2\pi} \frac{d^2N}{p_t dp_t dy} [1 + 2 \sum_{n=1}^{\infty} v_n \cos n(\phi - \psi_R)]. \end{aligned} \quad (95)$$

However, the orientation of the true reaction plane can only be measured with limited accuracy. Since fluctuations in a finite multiplicity environment result in azimuthal anisotropies without geometrical origin, this limited accuracy arises largely as a consequence of the basic statistical properties



of a mesoscopic system, and cannot be reduced by larger event samples or refined measurements. The resulting uncertainty has to be corrected for if one aims for a geometrical interpretation of the  $\Phi$ -dependence of HBT radius parameters. Such corrections are discussed in literature<sup>98,39</sup>.

### 3. Two-particle correlations from model calculations

The emission function  $S(x, K)$  is not determined uniquely by the correlator  $C(\mathbf{q}, \mathbf{K})$ . This is a consequence of the on-shell constraint (6) which implies that only a specific time-average over the emission function, the so-called relative distance distribution  $S_{\mathbf{K}}(\mathbf{x})$ , is uniquely measurable<sup>100</sup>

$$S_{\mathbf{K}}(\mathbf{x}) = \int dt d(\mathbf{x} + \beta t, t; K), \quad (96)$$

$$d(x, K) = \int d^4 X \frac{S(X + \frac{x}{2}, K)}{\int d^4 y S(y, K)} \frac{S(X - \frac{x}{2}, K)}{\int d^4 y S(y, K)}. \quad (97)$$

The direct reconstruction of  $S_{\mathbf{K}}(|\mathbf{x}|)$  from experimental data has been pursued successfully<sup>15,16,115</sup>. However, due to statistical uncertainties the numerical inversion of  $C(\mathbf{q}, \mathbf{K}) - 1 = \int d^3 \mathbf{x} \cos(\mathbf{q} \cdot \mathbf{x}) S_{\mathbf{K}}(\mathbf{x})$  is complicated. In practice, it requires additional model assumptions to achieve convergence. Thus most data analyses proceed via model studies. Either they start from a model parametrisation of the emission function  $S(x, K)$ , or they start from a dynamical calculation of  $S(x, K)$  based on a hydrodynamic or particle-cascade based simulation. In this section, we review the main features of these approaches.

#### 3.1. Model parametrisations of the emission function

The main features of the collision region at freeze-out can be characterised by its width in the different spatial and temporal extensions, its collective dynamical gradients (usually ascribed to a collective flow field  $u_\mu(x)$  which determines the position-momentum correlations in the source) and its random dynamical component (usually ascribed to a local temperature  $T$ ). Model parametrisations of  $S(x, K)$  implement these main features in a (minimal) analytical ansatz for  $S(x, K)$ . The model parameters are then extracted from a fit to one- and two-particle spectra.

Example of a model emission function: For illustration, consider a source in local thermal equilibrium at temperature  $T$  whose extension is given by the

transverse width  $R$ , space-time rapidity width  $\Delta\eta$  and proper longitudinal emission time  $\tau_0$  smeared with a width  $\Delta\tau$ . The transverse and longitudinal expansion of the collision system results in a longitudinally boost-invariant flow profile at freeze-out with a transverse component  $\eta_t(r) = \eta_f \frac{r}{R}$  characterised by the transverse gradient  $\eta_f$ ,

$$u_\mu(x) = (\cosh \eta \cosh \eta_t, \frac{x}{r} \sinh \eta_t, \frac{y}{r} \sinh \eta_t, \sinh \eta \cosh \eta_t) . \quad (98)$$

In longitudinal proper time  $\tau = \sqrt{t^2 - z^2}$  and rapidity  $\eta = \frac{1}{2} \ln [(t+z)/(t-z)]$ , this source can be written as<sup>2,19,24,96</sup>:

$$S_r(x, p) = \frac{2J_r + 1}{(2\pi)^3 \sqrt{2\pi} \Delta\tau} m_\perp \cosh(y - \eta) \exp \left[ -\frac{p \cdot u(x) - \mu_r}{T} \right] \\ \times \exp \left[ -\frac{r^2}{2R^2} - \frac{\eta^2}{2(\Delta\eta)^2} - \frac{(\tau - \tau_0)^2}{2(\Delta\tau)^2} \right] . \quad (99)$$

Here,  $r$  labels the particle species which are produced in thermal abundances with chemical potentials  $\mu_r$ . The model emission function (99) is completely specified by the model parameters  $T, \eta_f, R, \Delta\eta, \Delta\tau, \tau_0, \mu_r$ . This basic model allows for a satisfactory fit to experimental data from the CERN SPS<sup>89</sup>.

Overview of models and model extensions: In what follows, we review the physics arguments which motivated the study of modifications and extensions of the parameterisation (99):

- (1) Varying transverse density and flow profiles:

The functional shape of (99) was varied by replacing the Gaussian transverse density distribution with a box profile<sup>89</sup> or varying the functional dependence of the transverse flow profile<sup>95</sup>. This gives further support to the general statement that HBT radius parameters are mainly sensitive to the average r.m.s. width of  $S(x, K)$ . However, details in the functional shape of  $S(x, K)$  can leave observable traces in the  $K_\perp$  dependence of the HBT radii: in particular, experimental data from the SPS favour a transverse box profile over a Gaussian one.

- (2) Surface dominated versus bulk dominated emission:

Model (99) implements bulk emission, i.e., particles decouple at the same average proper freeze-out time  $\tau_0$  from all spatial positions in the source with a probability proportional to the source density. However, if reabsorption of particles by the surrounding matter is significant, hadronic freeze-out may proceed via surface evaporation. In analytical

parametrisations of  $S(x, K)$ , such “opaque sources” have been modelled via addition of absorption factors<sup>40</sup>. The main outcome of these studies is that surface-dominated emission can imply  $\langle \tilde{x}^2 \rangle \ll \langle \tilde{y}^2 \rangle$  and this makes it possible that  $R_o^2 < R_s^2$  at sufficiently large  $K_\perp$ .

(3) Temperature gradients:

Models which include a spatially varying local temperature attribute position-momentum correlations in the source to a combination of two different effects:  $T(x)$  and  $u_\mu(x)$ . This typically introduces two additional fit parameters<sup>24,87</sup> which characterise the longitudinal and transverse dependence of  $T(x)$ . It removes to some extent the constraint between temperature and transverse flow which can be exploited when fitting (99) to a combination of one- and two-particle spectra. Such a model was fitted successfully to first data from RHIC<sup>26</sup>.

(4) Model emission functions for finite impact parameter collisions:

The model (99) has been extended to azimuthally asymmetric transverse flow and asymmetric transverse Gaussian<sup>98</sup> or box geometry<sup>151</sup>. For the first and second harmonics of HBT radius parameters calculated in these models, explicit  $\Phi$ -dependence dominates over the implicit one and deviations from the purely geometrical identities (58) and (88) satisfy the dynamical identities (77) and (87), respectively. The latter point, however, is mainly a consequence of studying a class of models for which  $t$ -dependent space-time variances are  $\Phi$ -independent and azimuthal deformations are essentially elliptic.

Generic properties:

The analytical parametrisations reviewed above were instrumental in establishing how the main properties of the two-particle correlator translate into specific geometric or dynamical features of the collision region. The following generic properties emerge:

(1) Size and transverse momentum slopes of HBT radii:

Qualitatively, the main information contained in the absolute size and  $M_\perp$ -dependence of HBT radius parameters can be illustrated in terms of pocket formulas derived in a saddle point approximation of (99). For the side radius parameter one finds<sup>19</sup> for  $\Delta\eta = \infty$  and  $\Delta\tau = 0$

$$R_s^2(K_\perp) \approx \frac{R^2}{1 + \frac{M_\perp}{T} \eta_f^2}, \quad (100)$$

The size of this radius is proportional to the source size, but it is also sensitive to the transverse flow strength  $\eta_f$  of the source. This illustrates that HBT radii characterise only that part of a dynamically expanding source which can be viewed through a filter of wavelength  $K$ . This shrinking effect increases for increasing  $M_\perp$  proportional to the ratio  $\eta_f^2/T$ . The Makhlin-Sinyukov formula<sup>58</sup> for the longitudinal radius,

$$R_l^2 \approx \tau_0^2 \frac{T}{M_\perp}, \quad (101)$$

shows compared to (100) a stronger  $M_\perp$ -dependence consistent with the stronger longitudinal expansion implemented in (99). Its dependence on  $\tau_0$  is a direct consequence of the assumed longitudinal boost-invariance and receives corrections for sources of finite longitudinal extension.

While quantitative corrections to these analytical expressions can be significant<sup>95</sup>, these pocket formulas illustrate qualitatively the interplay of geometry and dynamics in determining HBT radius parameters. This picture is supported by numerous numerical studies.

- (2) The difference  $R_o^2 - R_s^2$ :

The main interest in this observable<sup>69</sup> lies in its sensitivity to the emission duration [see also discussion of eq. (120)]

$$R_o^2 - R_s^2 \approx \beta_\perp^2 \langle \tilde{t}^2 \rangle. \quad (102)$$

Numerical calculations with a Gaussian density profile typically result in a small but positive signal for  $R_o^2 - R_s^2$ . For steeper transverse profiles and particle emission at sufficiently large  $K_\perp$ , or for opaque source<sup>40,59</sup> models with surface dominated emission, also negative values can be found for  $R_o^2 - R_s^2$ . Equation (102) ignores the contribution from the  $\langle \tilde{x}\tilde{t} \rangle$  correlation term which vanishes in the model (99) but is present in hydrodynamic models and Monte Carlo event generators, see below.

- (3) Influence of resonance decay contributions:

Pions from resonance decays have a tendency to be emitted at later times and larger distances<sup>28,23,97</sup>. For models showing bulk emission, their effect on the size of HBT radius parameters is however small<sup>97</sup>. This is due to a combination of three effects: i) in models of the type (99), the emission region of the heavier resonances is smaller than that of direct pions, ii) the large decay widths of the most abundant resonances like  $\rho$ 's and  $\Delta$ 's and their non-relativistic velocities imply that these decays occur within the emission region of the direct pions, iii)

resonances with large lifetime ( $\eta, \eta'$ ) decay so far outside that their decay pions interfere with the directly produced ones on a very small relative momentum scale ( $|\mathbf{q}| < 1$  MeV) only. This produces a peak of the correlation function at  $|\mathbf{q}| < 1$  MeV which is narrower than the experimental resolution and thus leads to an apparently reduced intercept  $\lambda$  of the correlator  $C(\mathbf{q}, \mathbf{K})$  without affecting its shape. Only pions from  $\omega$  decays stem from a resonance which is neither sufficiently short-lived nor sufficiently long-lived and thus can affect the shape of the correlator. This spoils a naive core-halo interpretation and contributes to non-Gaussian deviations of the two-particle correlator<sup>96</sup>.

### 3.2. Hydrodynamic models

Hydrodynamic behaviour is an idealised but well-defined limiting case of the realistic dynamical evolution of the collision region in heavy ion collisions. It emerges as the zero mean free path limit of a particle cascade. In this limit, matter in the collision region is treated as an ideal, locally thermalised fluid whose dynamics is governed by the relativistic hydrodynamic equations.

Input for simulations: A hydrodynamic model is fully specified by the equation of state and the initial conditions. Typically, the parametrisation of the latter models the outcome of an initial pre-equilibrium stage with initial energy density estimated from the Glauber approach to entropy and energy production in nucleon-nucleon collisions<sup>49</sup>.

Freeze-out criterion: The freeze-out criterion, according to which the hydrodynamic simulation is terminated, is another important input in hydrodynamic model studies. Usually, the freeze-out criterion is set by a critical energy density or temperature. If the criterion is satisfied in a fluid cell, the cell is immediately assumed to freeze-out. Local properties of this cell are converted into a thermal ideal gas distribution of hadronic resonances with temperature and chemical potential set by the local energy and baryon density of the simulation. This leads to a sharp freeze-out along a three-dimensional hypersurface and specifies the emission function  $S(x, K)$  entering the calculation of two-particle correlation functions. There are “hybrid models” in which the earlier hot stage of the collision is treated hydrodynamically but the hadronic phase is modelled with a Monte Carlo event generator code<sup>80</sup>. An event generator naturally leads to an emission function in a finite four-volume, see next subsection.

Successes and problems at RHIC: At RHIC, hydrodynamic simulations

Table 2. The main hydrodynamic model calculations with published results on HBT correlation functions. Codes follow either the full three-dimensional expansion or the two-dimensional expansion in the transverse plane (with assumed boost-invariance in the remaining longitudinal direction).

Authors <sup>ref.</sup>	energies studied	HBT data compared to	Dim.
HYLANDER <sup>74,13</sup>	SPS	NA44 <sup>76</sup>	(3+1)-dim
Rischke, Gyulassy <sup>73</sup>	SPS, RHIC	RHIC prediction	(2+1)-dim
Zschesche <i>et al.</i> <sup>105</sup>	SPS, RHIC	NA49, STAR	(2+1)-dim
Kolb, Heinz <sup>38</sup>	RHIC	STAR, PHENIX <sup>38</sup>	(2+1)-dim
Hirano, Morita <i>et al.</i>	SPS, RHIC	NA49 <sup>61,62</sup> , STAR <sup>44,62</sup>	(3+1)-dim

compare in general well with the hadronic one-particle transverse momentum spectra up to  $\approx 2$  GeV. The major success of this approach is the prediction of the size of the measured elliptic flow  $v_2$ , as well as the correct description of its  $p_\perp$ -dependence for identified pion and proton spectra. This indicates that the main contribution to elliptic flow originates in the early stages of the collision where the system is very dense and the mean free path is close to the hydrodynamic limit zero. However, two-particle correlations are determined at freeze-out, where the mean free path (or rather the mean scattering time) is grown and a hydrodynamic picture becomes questionable. This may be one of the reasons why so far hydrodynamic simulations have significant problems in calculating two-particle correlators which are at least in qualitative agreement with experimental data<sup>38</sup>, see the following discussion.

Generic properties of hydrodynamic simulations for HBT: An overview of hydrodynamic model calculations is given in Table 2. This list is limited to studies which include beyond the calculation of one-particle spectra also two-particle correlation functions.

- (1) Freeze-out hyper-surface shows strong outward-temporal correlations: The freeze-out criterion implemented in hydrodynamic simulations amounts to a sudden switch from a zero mean free path to an infinite mean free path approximation. This tends to favour sharp geometrical correlations along the freeze-out hyper-surface. In comparison to model

sources with emission from a finite four-volume, the  $\langle \hat{x}\hat{t} \rangle$  variance is significantly stronger<sup>72</sup>. Thus, the difference  $R_o^2 - R_s^2$  does not measure a lifetime effect only. This consequence of a sharply localised freeze-out hyper-surface may be tamed in hybrid models in which hydrodynamic evolution is followed by a hadronic rescattering phase<sup>80</sup>.

- (2) Large “lifetime” effect and  $R_o^2 \gg R_s^2$ :

Hydrodynamic simulations lead to sources with very large emission durations. The size of this lifetime signal depends on the equation of state (EOS): a softer EOS results in a more delayed pressure build-up and a longer lifetime<sup>72,73</sup>. Irrespective of model details, the resulting values for  $R_o/R_s$  are generically much larger than the measured result<sup>38</sup>. This is the main problem of hydrodynamic simulations.

- (3) Resonance decays contribute significantly to HBT radii:

In contrast to model sources of the type (99), resonance decay contributions added to the freeze-out of hydrodynamic simulations were reported to increase the size of HBT radii significantly<sup>13</sup>. This may be attributed to the different shapes of the freeze-out hyper-surfaces. The homogeneity regions for direct pion and resonance emission are the same in hydrodynamic simulations whereas the latter are smaller in the model (99). Thus even short-lived resonance decay contributions tend to increase the hydrodynamic pion source.

### 3.3. Monte Carlo event generators

Event generators are widely used to simulate particle production in ultra-relativistic heavy ion collisions. In particular, they allow to study how global collective dynamical properties emerge in a mesoscopic system from microscopic (2-to-2 or 2-to-3 body) interactions. In principle, each event generator output defines an emission function from which two-particle correlations can be calculated. However, since the event generator output is not a wavefunction with proper quantum-mechanical symmetrisation, an additional prescription is needed of how to relate it to the emission function. There is an extensive literature on the conceptual problem<sup>100</sup>. In practice, the afterburner program of Scott Pratt<sup>70</sup> is most frequently used.

So far, there are only very few calculations of HBT correlation functions from event generators, see Table 3. The main conclusion from these calculations is that the late hadronic rescattering phase largely determines the size

Table 3. Event generator model calculations with published results on HBT correlation functions.

Code <sup>ref.</sup>	energies studied	HBT data compared to
RQMD <sup>83,84,a</sup>	SPS	NA35 <sup>86</sup>
hydro <sup>73</sup> +URQMD <sup>6,b</sup>	SPS, RHIC <sup>80,81</sup>	STAR <sup>82</sup>
Humanic <sup>45,c</sup>	AGS, SPS, RHIC	E859/866, NA44 <sup>46</sup> STAR <sup>47</sup>
AMTP <sup>56,d</sup>	RHIC	STAR <sup>56</sup>
MPC <sup>60</sup>	RHIC	STAR, PHENIX <sup>60</sup>

<sup>a</sup> Code not maintained any more, no more recent studies available.

<sup>b</sup> Hadronic rescattering phase dominates HBT radii<sup>82</sup>.

<sup>c</sup> This code models final state rescattering only.

<sup>d</sup> This is a multi-phase transport model which includes initial partonic and final state hadronic interactions.

of HBT radius parameters. Also, in contrast to hydrodynamic models, the generation of models with relatively small lifetime, satisfying  $R_o/R_s \sim 1$ , does not appear to be a fundamental problem. While some simulations find a ratio  $R_o/R_s$  which for large  $K_\perp$  lies between 1.4 and 2.0, inconsistent with experimental data<sup>82</sup>, other simulations<sup>47,56</sup> are consistent with  $R_o/R_s \sim 1$ .

#### 4. HBT measurements

Two-particle correlations have been measured at all energies from AGS to RHIC. Here we give an overview of the experimental situation.

##### 4.1. Coulomb final state corrections

Data on two-particle momentum correlations between identical charged pions are usually corrected by the experimentalists for the pairwise Coulomb repulsion. These corrections are difficult since Coulomb interaction and Bose-Einstein interference effects are of similar size and affect the two-particle correlator on similar relative momentum scales. Moreover, the used correction methods differ between experiments and sometimes even between different publications in one experiment. Differences between the used correction techniques can change the resulting size of the HBT radius parameter by more than 1 fm and they may affect the  $K_\perp$ -slope of HBT radii.



Thus Coulomb final state corrections are a major source of systematic uncertainty in the space-time analysis of correlation measurements.

The final state Coulomb interaction between two charged particles is described by the relative Coulomb wave-function of the particle pair, written in terms of the confluent hypergeometric function  $F$ <sup>53,67</sup>,

$$\Phi_{\mathbf{q}/2}^{\text{coul}}(\mathbf{r}) = \Gamma(1 + i\eta) e^{-\frac{1}{2}\pi\eta} e^{\frac{i}{2}\mathbf{q}\cdot\mathbf{r}} F(-i\eta; 1; z_-), \quad (103)$$

$$z_{\pm} = \frac{1}{2}(qr \pm \mathbf{q} \cdot \mathbf{r}) = \frac{1}{2}qr(1 \pm \cos\theta). \quad (104)$$

Here,  $r = |\mathbf{r}|$ ,  $q = |\mathbf{q}|$ , and  $\theta$  denotes the angle between these vectors. The Sommerfeld parameter  $\eta = \alpha/(v_{\text{rel}}/c)$  depends on the particle mass  $m$  and the electro-magnetic coupling strength  $e$ . We write

$$\eta_{\pm} = \pm \frac{e^2}{4\pi} \frac{\mu}{q/2} = \pm \frac{m e^2}{4\pi q}, \quad (105)$$

where  $\mu$  is the reduced mass and the plus (minus) sign is for pairs of unlike-sign (like-sign) particles. If particle pairs are emitted from a *static* source at initial relative distance  $\mathbf{r}$  with a probability  $S_{\text{stat}}(\mathbf{r}; \mathbf{K})$ , then the corresponding correlation is given by an average over the squared wave-function (103),

$$C(\mathbf{q}, \mathbf{K}) = \int d^3r S_{\text{stat}}(\mathbf{r}; \mathbf{K}) |\Phi_{\mathbf{q}/2}^{\text{coul}}(\mathbf{r})|^2. \quad (106)$$

In the case of identical particles, the two-particle symmetrised version of (103) should enter equation (106). The  $\mathbf{K}$ -dependence of the pair emission probability is often neglected when calculating Coulomb corrections.

The following Coulomb correction methods are based on this starting point:

(1) Point-like Gamow Correction

For a point-like source  $S_{\text{stat}}(\mathbf{r}) = \delta^{(3)}(\mathbf{r})$ , the correlator (106) is given by the Gamow factor  $G(\eta)$

$$G(\eta) = \left| \Phi_{\mathbf{q}/2}^{\text{coul}}(0) \right|^2 = \frac{2\pi\eta}{e^{2\pi\eta} - 1}. \quad (107)$$

Early studies constructed the corrected like-sign two-particle correlation by dividing the measured correlator by this Gamow factor

$$C_{\text{corr}}^{(--)}(\mathbf{q}, \mathbf{K}) = C_{\text{meas}}^{(--)}(\mathbf{q}, \mathbf{K})/G(\eta_-). \quad (108)$$

(2) Static Finite Size Correction

The point-like Gamow correction (107) largely overestimates the real effect of Coulomb corrections since particles are emitted in reality with finite separation  $\mathbf{r}$  which leads to a weaker Coulomb interaction. An improvement advocated repeatedly<sup>67,14,7</sup> is to calculate the correction factor for a finite size static source. Typically, a Gaussian ansatz  $S_{\text{stat}}(\mathbf{r}) \propto \exp[-\mathbf{r}^2/4R^2]$  is chosen in (106),

$$F_{\text{corr}}^{\text{stat}}(\mathbf{q}) = \int d^3r S_{\text{stat}}(\mathbf{r}) |\Phi_{\mathbf{q}/2}^{\text{coul}}(\mathbf{r})|^2, \quad (109)$$

$$C_{\text{corr}}^{(--)}(\mathbf{q}, \mathbf{K}) = C_{\text{meas}}^{(--)}(\mathbf{q}, \mathbf{K}) / F_{\text{corr}}^{\text{stat}}(\mathbf{q}). \quad (110)$$

Instead of the analytical emission function in eq. (109), the particle-emitting source can be characterized in terms of a discrete set of phase-space points obtained e.g. from a Monte Carlo simulation. In this case, the correlation due to particle symmetrization and final state interactions is usually calculated with a so-called afterburner routine. The most widely used afterburner is Scott Pratt's CRAB<sup>70</sup> (CoRrelation After-Burner).

In practice, the value for the source width  $R$  in eq. (109) is determined iteratively from the extracted HBT radius parameter in the fitting procedure. A finite purity of the sample due to misidentified particle leads to an overall correlation strength  $\Lambda < 1$ . This can be taken into account by generalising<sup>78</sup> eq. (110) to

$$C_{\text{meas}}^{(--)}(\mathbf{q}, \mathbf{K}) = (1 - \Lambda) + \Lambda C_{\text{corr}}^{(--)}(\mathbf{q}, \mathbf{K}) F_{\text{corr}}^{\text{stat}}(\mathbf{q}). \quad (111)$$

(3) Correction of like-sign by unlike-sign correlations

Rather than to calculate Coulomb corrections for finite size sources, one can make use of the fact that unlike-sign correlations receive no contribution from Bose-Einstein symmetrisation effects but depend on Coulomb correlations of the same magnitude (but opposite sign),

$$C_{\text{corr}}^{(--)}(\mathbf{q}, \mathbf{K}) = C_{\text{meas}}^{(+-)}(\mathbf{q}, \mathbf{K}) C_{\text{meas}}^{(--)}(\mathbf{q}, \mathbf{K}). \quad (112)$$

Theoretical support for this procedure comes from the fact, that like-sign and unlike-sign Coulomb correlations calculated from (106) compensate largely. For point-like sources, e.g., the product of the Gamow factors deviates from unity by less than five percent for relative mo-

menta  $q > 8 \frac{m}{137}$

$$G(\eta_+) G(\eta_-) = \frac{1}{1 + (\pi^2/3)\eta^2 + O(\eta^4)}. \quad (113)$$

A further improvement over (112) is to take this deviation into account<sup>78</sup>,

$$C_{\text{corr,improved}}^{(--)}(\mathbf{q}, \mathbf{K}) = \frac{C_{\text{meas}}^{(+-)}(\mathbf{q}, \mathbf{K}) C_{\text{meas}}^{(--)}(\mathbf{q}, \mathbf{K})}{G(\eta_+) G(\eta_-)}. \quad (114)$$

This was shown to work with excellent accuracy for a wide range of source parameters<sup>78</sup>.

The effects of finite momentum resolution reduce both  $C_{\text{meas}}^{(+-)}(\mathbf{q}, \mathbf{K})$  and  $C_{\text{meas}}^{(--)}(\mathbf{q}, \mathbf{K})$ . As an unwanted consequence, these effects are amplified in the product defining the corrected like-sign correlation functions (112) and (114). An empirical parametrization which takes into account finite momentum resolution is discussed below; see eq. (117).

(4) Experimental parametrisations of Coulomb corrections

Unlike-sign correlations  $C_{\text{meas}}^{(+-)}(\mathbf{q}, \mathbf{K})$  were parametrised by the function<sup>120</sup>

$$F(q_{\text{inv}}) = 1 + (G(\eta_+) - 1) e^{-q_{\text{inv}}/Q_0}, \quad (115)$$

which depends on

$$q_{\text{inv}} = \sqrt{\mathbf{q}^2 - (q^0)^2}. \quad (116)$$

The parameter  $Q_0$  is extracted from the fit. It quantifies a phenomenological finite-size correction for large relative momentum. The function  $F(q_{\text{inv}})$  approaches the Gamow factor (107) for a point-like source,  $Q_0 \rightarrow \infty$ .

In order to take into account the imperfect purity of the sample and the finite experimental momentum resolution, CERES<sup>132</sup> parametrised the Coulomb correction by

$$C_{\text{meas}}^{(--)}(\mathbf{q}, \mathbf{K}) = (1 - \lambda) + \lambda C_{\text{corr}}^{(--)} [w_{K_\perp} (F_{\text{coul}}(q_{\text{inv}}) - 1) + 1]. \quad (117)$$

In a Monte Carlo simulation of the final momentum resolution, the Coulomb correction function  $F_{\text{coul}}(q_{\text{inv}})$  was obtained by evaluating eq. (109) and reducing  $F_{\text{corr}}^{\text{stat}}(\mathbf{q})$  accordingly. The same Monte Carlo simulation determines  $w_{K_\perp}$  which accounts for the depletion of the parameter  $\lambda$  due to finite momentum resolution effects. This is chosen

such that  $\lambda w_{K_\perp}$  gives the “true” corrected intercept parameter, which then multiplies the correction factor  $(F_{\text{coul}}(q_{\text{inv}}) - 1)$ . For perfect momentum resolution,  $w_{K_\perp} \rightarrow 1$  and  $F_{\text{coul}}(q_{\text{inv}}) \rightarrow F_{\text{corr}}^{\text{stat}}(q_{\text{inv}})$ , and the prescription (117) agrees with (111).

The above discussion is mainly for static sources and involves  $q_{\text{inv}}$ -dependent correction factors only. In principle, Coulomb correction effects are different for the different relative momentum components, as seen from eq. (109). For dynamically expanding sources, a formalism for the calculation of Coulomb corrections exists<sup>4</sup>, but it has not been used so far in comparison to data. Only one of the correction methods listed above, eq. (112), contains some information about expansion effects since it uses the measured unlike-sign correlation as correction factor.

#### 4.2. Experiments at the Alternating Gradient Synchrotron (AGS)

At the AGS of the Brookhaven National Laboratory (BNL) three series of collaborations have measured and published results on Bose-Einstein correlations in fixed target experiments with beam energies varying between 2 AGeV and 11.6 AGeV. Due to lack of statistics, measured correlation functions were parametrised often by a 1-dimensional parametrisation

$$C(q_{\text{inv}}) = 1 + \lambda e^{-q_{\text{inv}}^2 R_{\text{inv}}^2}, \quad (118)$$

where the invariant momentum difference  $q_{\text{inv}}$  is defined in eq. (116).

*E802/E859/E866/E917* These experiments use a rotating spectrometer (the “Henry Higgins” Spectrometer) which in the E866 upgrade was supplemented by a Forward Spectrometer. The acceptance is at or close to mid-rapidity. The E802/E859/E866 Collaboration has published a systematic study of the dependence of HBT radius parameters on transverse mass  $M_\perp = \sqrt{m^2 + \mathbf{K}_\perp^2}$ , system size and centrality dependences<sup>107</sup>. The last of the series, the E917 experiment, collected HBT data on beam energy dependence in Au+Au collisions from 6 to 10.6 AGeV. At the time of this writing, these data are still preliminary<sup>117</sup>.

*E895* This experiment uses the EOS time projection chamber inherited from Bevalac<sup>112</sup>. BE correlations were measured in 2, 4, 6, and 8 AGeV

Table 4. BE correlation data available from AGS experiments. Data are taken at mid-rapidity, are finite size Coulomb corrected and are in Bertsch-Pratt parametrisation, unless noted otherwise. The fourth column indicates the analysis frame and the fifth column denotes whether the cross-term was included in the fits (yes), not included (no), checked to be 0 and then not included (0) or was not applicable since a simpler parametrisation was used (N/A).

<b>Au+Au collisions</b>					
impact energy	collab. <sup>ref.</sup>	$K_{\perp}$ and binning	frame	cross-term	note
2 AGeV/ $\sqrt{s} = 2.4$ AGeV	E895 <sup>114</sup>	0.1-0.3 GeV/c, 3 bins	CMS	0	at midrapidity CMS=LCMS
4 AGeV $\sqrt{s} = 3.1$ AGeV	E895 <sup>114</sup>	0.1-0.3 GeV/c, 3 bins	CMS	0	at midrapidity CMS=LCMS
6 AGeV $\sqrt{s} = 3.6$ AGeV	E895 <sup>114</sup> E917 <sup>117</sup>	0.1-0.3 GeV/c, 3 bins	CMS –	0 N/A	at midrapidity CMS=LCMS preliminary data of $R_{\text{inv}}$
8 AGeV $\sqrt{s} = 4.1$ AGeV	E895 <sup>114</sup> E917 <sup>117</sup>	0.1-0.3 GeV/c, 3 bins	CMS –	0 N/A	at midrapidity CMS=LCMS preliminary data of $R_{\text{inv}}$
10.6 AGeV $\sqrt{s} = 4.7$ AGeV	E917 <sup>117</sup>		–	N/A	preliminary data of $R_{\text{inv}}$
10.8 AGeV $\sqrt{s} = 4.7$ AGeV	E877 <sup>110</sup> E877 <sup>109</sup>	0-0.5 GeV/c, 1 bin $\langle p_{\perp} \rangle = 0.1$ GeV/c 1 bin	beam rapidity –	yes N/A	data at beam rapidity prelim. $R_{\text{inv}}$ from $K^+K^+$
11.6 AGeV $\sqrt{s} = 4.9$ AGeV	E802 <sup>107</sup>	3 bins, $\langle m_{\perp} \rangle =$ 0.29, 0.4, 0.54 AGeV/c	YK frame	yes	
<b>Si+X collisions at 14.6 AGeV</b>					
target	collab. <sup>ref.</sup>	$K_{\perp}$ and binning	frame	cross-term	note
Pb	E814 <sup>108</sup>	1 bin	–	N/A	$R_{\text{inv}}$ , beam rap., Gamow
Al	E802 <sup>107</sup>	1 bin	YK frame	yes	
Au	E802 <sup>107</sup>	3 for $\pi^-$ :	YK frame	yes	
	E802/E859 <sup>106</sup>	2 for $\pi^+$ 1 bin	CMS	no	prelim. $K^+K^+$ , Gamow corr.

HBT from AGS to RHIC

Au+Au collisions. Published data exist for the transverse mass dependences of correlation radii<sup>114</sup>, and the azimuthal dependences in non-central collisions for the three lower energies<sup>113</sup>. Results on average phase-space density as a function of  $K_{\perp}$  and beam energy were shown at the Quark Matter 2001 conference<sup>116</sup>. All published data are at mid-rapidity.

*E814/E877* Particle correlations at projectile rapidity were measured with the Forward Magnetic Spectrometer of the E814/E877 Collaboration. The E814 is a Si-beam experiment<sup>108</sup> while E877 measured Au+Au at 10.8 AGeV<sup>110</sup>. E877 determined the pion phase-space density at freeze-out for the latter system<sup>110</sup>. At the Quark Matter 97 conference, they showed a direct fit of a Gaussian core-halo source function to  $K_{\perp}$  and  $y$ -binned correlation function and extracted source radii for pions and for kaons<sup>111</sup>.

A summary of AGS experiments is given in Table 4.

#### **4.3. Experiments at the CERN Super Proton Synchrotron (SPS)**

The CERN SPS was used first to accelerate  $^{16}\text{O}$  and  $^{32}\text{S}$  nuclei to 200 AGeV. Then it was upgraded to accelerate a 158 AGeV  $^{208}\text{Pb}$  beam. Recently, the CERN SPS delivered Pb-beams at lower energies: 40 and 80 AGeV. The step-by-step improvement of analysis tools during the CERN SPS heavy ion program is clearly seen in the available data. The correlation measurements for oxygen and sulphur beams were parametrised first in terms of  $q_{\text{inv}}$  only. The later three-dimensional fits do not include the cross-term (18). Also, the Coulomb repulsion was corrected initially by multiplying with a Gamow factor which overestimates the repulsion significantly. Improved Coulomb corrections, based on averaging the squared Coulomb wave function over a finite source size, were only introduced approximately with the arrival of the Pb beam.

*NA35* Originally, this experiment used a large streamer chamber in a magnetic field to measure tracks of charged particles and their momenta in O+Au collisions. The large volume of the detector allowed for the study of three rapidity windows between  $-2.4$  and  $1.6$  in the CMS of the nucleon-nucleon collision<sup>118</sup>. Due to small statistics, the correlation function was

Table 5. BE correlations data for central oxygen-induced reactions at 200 AGeV/c. All correlation functions are constructed from hadron pairs and are corrected for final state interactions by the Gamow factor. The parametrisations used by both experiments are listed in the last column. They include an additional factor 1/2 in the exponent of the correlation function.

target	collab.ref.	rapidity	frame	$K_{\perp}$	param.
C Cu Ag Au	WA80 <sup>142</sup>	$-1 < y_{\text{lab}} < 1$	lab	40 – 200 MeV/c	$q_{\text{inv}}$ and 2d: $q_{\perp}, q_l$
Au	NA35 <sup>120</sup>	$0.5 < y_{\text{lab}} < 3.5$ 3 bins	CMS	50 – 600 MeV/c	BP no cross-term

parametrised in  $q_l = q_{\text{long}}$  and  $q_{\perp} = \sqrt{q_o^2 + q_s^2}$ ,

$$C(q) = 1 + \lambda \exp \left[ -\frac{1}{2} q_l^2 R_l^2 - \frac{1}{2} q_{\perp}^2 R_{\perp}^2 \right]. \quad (119)$$

In contrast to other experiments, this parametrisation used by NA35 has an additional factor 1/2 in the exponent. The NA35 detector does not identify pions. Thus NA35 always studied hadron-hadron correlations. With the O-induced collisions a measurement of “single-event interferometry”<sup>119</sup> was attempted. For measurements with the sulphur beam, the detector was upgraded with a time projection chamber (TPC) which was crucial in gaining good statistics for correlation analysis. In a comprehensive study<sup>120</sup> of S-induced reactions with C, S, Cu, Ag, and Au targets, NA35 measured the rapidity,  $K_{\perp}$ , and multiplicity dependence of Bertsch-Pratt correlation radii. O+Au results were reanalysed in this work with better statistics. The  $K_{\perp}$  dependence of correlation radii was also reported in a letter<sup>121</sup>. Although the existence of a sizeable cross-term was first confirmed by NA35<sup>122</sup>, no results with the cross-term were published.

*NA49* For the lead beam, this collaboration equipped the NA35 detector with four large TPCs which allow for precise tracking of the secondaries in the rapidity region  $2 < y < 5.5$  (values given in the laboratory system with  $y_{\text{CMS}} = 2.9$  for the 158 AGeV Pb beam). The NA49 detector is able to identify particles by a combination of energy loss and time-of-flight measurements. So far, however, only unidentified hadron-hadron correlations

Table 6. BE correlation data for central sulphur-induced reactions at 200 AGeV. In all cases, final state interactions are corrected for by the Gamow factor. None of the parametrisations listed in the sixth column includes the cross term in the BP parametrisation.

target	collab. <sup>ref.</sup>	rapidity	frame	$K_{\perp}$	param.	note
C	NA35 <sup>120</sup>	$2.5 < y_{\text{lab}} < 4.5$ , 2 bins	CMS	$50 - 600 \text{ MeV}/c$	BP	factor 1/2 in the exponent
S	NA35 <sup>120</sup>	$0.5 < y_{\text{lab}} < 3.5$ , 3 bins	CMS	$50 - 600 \text{ MeV}/c$ <sup>a</sup>	BP	factor 1/2 in the exponent
	NA44 <sup>127</sup>	$y_{\text{lab}} \approx 3$	LCMS	$K_{\perp} \leq 400 \text{ MeV}/c$	BP	
Al	WA80 <sup>142</sup>	$-1 < y_{\text{lab}} < 1$	lab	$40 - 200 \text{ MeV}/c$	2 dim: $q_{\perp}, q_l$	factor 1/2 in the exponent
Cu	NA35 <sup>120</sup>	$2.5 < y_{\text{lab}} < 4.5$ , 2 bins	CMS	$50 - 600 \text{ MeV}/c$ <sup>a,b</sup>	BP	factor 1/2 in the exponent
Ag	NA35 <sup>120</sup>	$0.5 < y_{\text{lab}} < 4.5$ , 4 bins	CMS	$50 - 600 \text{ MeV}/c$ <sup>c</sup>	BP	factor 1/2 in the exponent
	NA44 <sup>127</sup>	$y_{\text{lab}} \approx 3$	LCMS	$K_{\perp} \leq 400 \text{ MeV}/c$	2 dim: $q_{\perp}, q_l$	
Pb	NA44 <sup>126</sup>	$y_{\text{lab}} \approx 3$	LCMS	2 bins <sup>d</sup>	BP	
	NA44 <sup>124</sup>	$y_{\text{lab}} \approx 3$	LCMS	2 bins <sup>e</sup>	BP <sup>f</sup>	kaon interferometry
Au	NA35 <sup>120</sup>	$0.5 < y_{\text{lab}} < 4.5$ , 4 bins	CMS	$50 - 600 \text{ MeV}/c$ <sup>a,b</sup>	BP	factor 1/2 in the exponent
	WA80 <sup>142</sup>	$-1 < y_{\text{lab}} < 1$	lab	$40 - 200 \text{ MeV}/c$	2 dim: $q_{\perp}, q_l$	factor 1/2 in the exponent

<sup>a</sup> The  $K_{\perp}$  dependence of correlation radii was measured for  $3.5 < y_{\text{lab}} < 4.5$ .

<sup>b</sup> The  $K_{\perp}$  dependence of correlation radii for  $2.5 < y_{\text{lab}} < 3.5$  was also published<sup>121</sup>.

<sup>c</sup> The  $K_{\perp}$  dependences of correlation radii were measured in all rapidity bins.

<sup>d</sup> The two NA44  $K_{\perp}$  bins correspond to  $\langle p_{\perp} \rangle \approx 150$  and  $450 \text{ MeV}/c$  respectively.

<sup>e</sup> For the BP parametrisation, the two bins correspond to  $\langle p_{\perp} \rangle \approx 163$  and  $246 \text{ MeV}/c$  respectively.

<sup>f</sup> Results from other parametrisations are also available<sup>124</sup>.



Table 7. BE correlation data for Pb+Pb collisions at the SPS. Correlation radii were measured as functions of  $K_{\perp}$  and the cross-term was included in the parametrisations. The fifth column (FSI) specifies how final state interactions are corrected for by referring to the corresponding relation in Section 4.1. The column on particle identification (PID) specifies whether measurements are for identified pions (YES) or charged hadrons (NO).

collab.ref.	frame	rapidity	param.	FSI	PID	note
NA44 <sup>128,131</sup>	LCMS	central <sup>a</sup>	BP	(110)	yes	also kaon interferometry <sup>131</sup>
NA45 <sup>132</sup>	LCMS	central	BP	(117)	no	measured for Pb+Au @ 40, 80, 158 AGeV/c
NA49 <sup>134,135,137</sup>	FLCMS	$0.1 < y_{\text{CMS}} < 2.1$ 4 bins	YKP, BP	$(115)^{134,135}$ , $(112)^{135}$ , $(117)^{137}$	no	40, 80, 158 AGeV/c <sup>137</sup> also kaon interferometry <sup>139</sup>
WA97 <sup>143</sup>	LCMS	$-0.3 < y_{\text{CMS}} < 0.9$ 4 bins	YKP, BP	iterative (110) <sup>b</sup>	no	
WA98 <sup>144,146</sup>	LCMS	$-0.8 < y_{\text{CMS}} < 0.2^c$	BP, YKP	iterative (110)	yes	

<sup>a</sup> NA44 has a “banana-shaped” acceptance around midrapidity. Small- $p_{\perp}$  data are at slightly forward, high- $p_{\perp}$  data at slightly backward rapidity.

<sup>b</sup> In determining the Coulomb correction  $F_{\text{corr}}(\mathbf{q})$  from eq. (109) WA97 iteratively used the emission function (99) instead of a static Gaussian distribution.

<sup>c</sup> WA98 has a “banana-shaped” acceptance at slightly backward rapidity. High- $p_{\perp}$  data are further away from midrapidity.

Table 8. Data on the centrality dependence of correlation radii.

collab. <sup>ref.</sup>	system and energy	rapidity
E802 <sup>107</sup>	Si+Al @ 14.6 AGeV Si+Au @ 14.6 AGeV Au+Au @ 11.6 AGeV	mid-rapidity
NA35 <sup>120</sup>	S+Ag @ 200 AGeV	$-2.5 < y_{\text{CMS}} < 1.5$ , 4 bins
NA44 <sup>127</sup>	S+S, S+Ag, S+Pb @ 200 AGeV	mid-rapidity
NA45 <sup>132</sup>	Pb+Au @ 40, 80, 158 AGeV	mid-rapidity
NA49 <sup>136,138</sup>	Pb+Pb @ 40, 80, 158 AGeV	$y_{\text{CMS}} = 0^{138}, 1.3^{136}$
WA97 <sup>143</sup>	Pb+Pb @ 158 AGeV	$-0.3 < y_{\text{CMS}} < 0.9$
STAR <sup>150,153</sup>	Au+Au @ $\sqrt{s} = 130$ AGeV <sup>150</sup> $\sqrt{s} = 200$ AGeV <sup>153</sup>	mid-rapidity
PHENIX <sup>148</sup>	Au+Au @ $\sqrt{s} = 200$ AGeV	mid-rapidity

are available. For Pb+Pb collisions at 158 AGeV, the rapidity and  $K_{\perp}$  dependence of YKP parameters was published<sup>134</sup>. Also, a rather comprehensive compilation of preliminary data at all rapidities and in both YKP and Bertsch-Pratt is available<sup>135</sup>. Preliminary results<sup>137,138</sup> exist for  $h^-h^-$  correlations in 40, 80, and 158 AGeV Pb+Pb collisions with different centralities. Results for kaon-kaon correlations in central 158 AGeV Pb+Pb collisions were published very recently<sup>139</sup>. These latter studies are the only ones based on “global tracking” for which tracks from all TPCs are matched before constructing the correlation function.

*NA44* This experiment is based on a focusing spectrometer. Its narrow acceptance is around mid-rapidity and depends in detail on the detector setting which may be varied. The performance is optimised for particles with small momentum difference and good particle identification is achieved. For the S-beam, one-dimensional correlation functions for S+Pb collisions<sup>123</sup>, and a kaon interference study<sup>124</sup> were published first. Bertsch-Pratt radii without the cross-term were published in 1995<sup>125</sup> and a dedicated paper was written on their  $M_{\perp}$  dependence<sup>126</sup>. NA44 studied collisions with other

Table 9. Data on three-pion interferometry.

collab. <sup>ref.</sup>	system and energy	rapidity
NA44 <sup>129</sup>	S+Pb @ 200 AGeV	mid-rapidity
WA98 <sup>145,146</sup>	Pb+Pb @ 158 AGeV	$-0.8 < y_{\text{CMS}} < 0.2$ $\langle y_{\text{CMS}} \rangle = -0.2$
STAR <sup>154</sup>	Au+Au @ $\sqrt{s} = 130$ AGeV	mid-rapidity

Table 10. Data on the azimuthally dependence of HBT radius parameters. All data are taken at central rapidity.

collab. <sup>ref.</sup>	$\phi$ -dependent radii	system and energy
E895 <sup>113</sup>	all six radii $R_{ij}^2(\phi)$	Au+Au @ 2, 4, 6 AGeV
STAR <sup>153</sup>	$R_o^2, R_s^2, R_{os}^2, R_l^2$	Au+Au @ $\sqrt{s} = 130, 200$ AGeV

targets<sup>127</sup>: S+S, S+Ag, S+Pb. More recently an investigation of three-particle correlations in S+Pb systems was published<sup>129</sup>.

There are two papers with data from the 158 AGeV Pb+Pb collisions, one for pion<sup>128</sup>, and one for kaon<sup>131</sup> interferometry. These study the  $M_\perp$  dependence of the BP correlation radii within the limited acceptance of the detector.

*NA45-CERES* In 1998, the CERES collaboration upgraded their detector with a time projection chamber with radial drift field. This allows for interferometric studies. CERES measured correlations of non-identified hadrons in Pb+Au collisions at 40, 80 and 158 AGeV with various centralities<sup>132</sup>.

*WA80* The correlation analysis of WA80 is based on the so-called plastic ball detector which has coverage in the target rapidity region and at low  $p_\perp < 220$  MeV/c. For the oxygen beam they used C, Cu, Ag, and Au targets. The sulphur beam was collided with Al and Au targets, the proton beam at 450 AGeV/c was collided with C and Au targets. An earlier analysis of target dependence of the observed HBT radii for O-induced

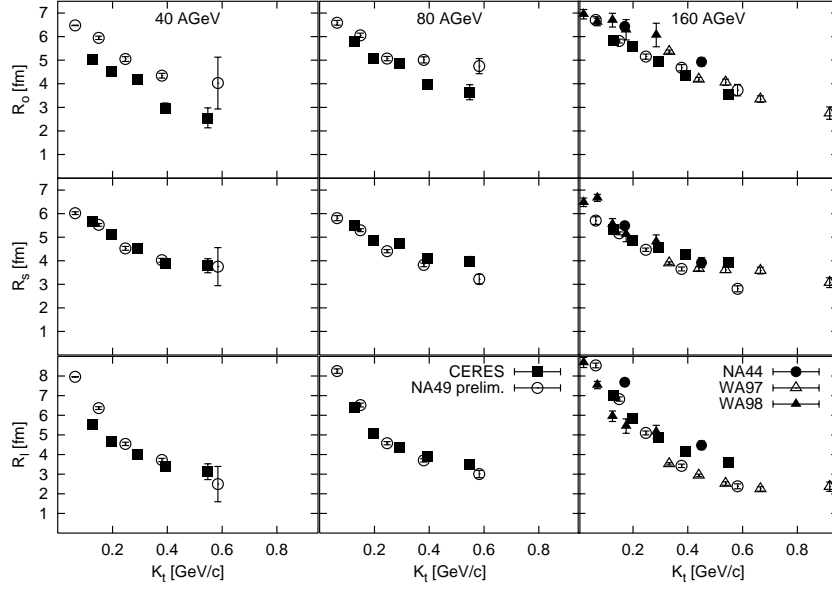


Fig. 6. Summary of the  $K_{\perp}$ -dependence of correlation radii measured at the CERN SPS in Pb+Pb collisions at midrapidity. Data are taken from NA44<sup>128</sup>, CERES<sup>132</sup>, preliminary NA49<sup>137</sup>, WA97<sup>143</sup> and WA98<sup>146</sup>.

reactions<sup>140</sup> was superseded by a study including also S and p as projectiles in which the detector performance correction was better understood<sup>142</sup>. The latter paper also shows a simple model fit to the correlation function with Coulomb correction (110) instead of Gamow factor multiplication (108). They used an additional factor of 1/2 in the correlation function like NA35 did. Another work<sup>141</sup> analyses these data in the context of intermittency.

**WA98** For the lead beam runs, this collaboration made use of the plastic ball calorimeter. To measure charged particles the detector includes a two arm tracking spectrometer with “banana-shaped”  $\pi^-$  acceptance around mid-rapidity. WA98 published a study of the  $K_{\perp}$  dependence of correlation radii for identified  $\pi^-$  in Bertsch-Pratt and YKP parametrisations<sup>144,146</sup>. Three pion interferometry<sup>145,146</sup> and pion phase-space density<sup>146</sup> were also studied.

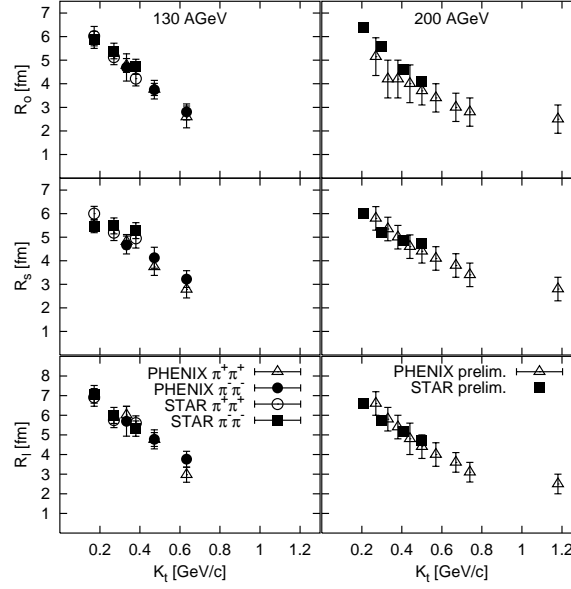


Fig. 7. Summary of the  $K_{\perp}$ -dependence of correlation radii at mid-rapidity measured at RHIC in Au+Au collisions. Data are taken from STAR<sup>150,153</sup> and PHENIX<sup>147,148</sup>. Data for  $\sqrt{s} = 200$  AGeV are taken from transparencies shown at the Quark Matter 2002 conference.

*WA97* To measure BE correlations, WA97 used a silicon telescope which provides precise tracking of produced particles within the magnetic field. They do not identify particle species but sample the correlation function with  $h^-h^-$  pairs. The data are mainly presented in the YKP parametrisation but consistency checks with the Bertsch-Pratt form were performed<sup>143</sup>. Transverse momentum and rapidity dependences of the correlation radii were investigated in the acceptance window  $-0.3 < y < 0.9$  (in CMS) and  $0.2 \text{ GeV}/c < p_{\perp} < 1.3 \text{ GeV}/c$ .

#### 4.4. Experiments at the Relativistic Heavy Ion Collider (RHIC)

Three of the four collaborations at RHIC published results on BE interferometry: STAR, PHENIX, and PHOBOS. Data were taken from Au+Au collisions at CMS energies of 130 and 200 AGeV.

*STAR* uses a time projection chamber in a solenoidal magnetic field. The analysis for  $\sqrt{s} = 130$  AGeV<sup>150</sup> covers in three bins the  $K_\perp$ -dependence from 0.125 GeV/ $c$  to 0.45 GeV/ $c$  within a rapidity region  $|y_{\text{CMS}}| < 0.5$ . Preliminary data at  $\sqrt{s} = 200$  AGeV range in four bins up to  $K_\perp \approx 0.52$  GeV/ $c$ <sup>153</sup>. The centrality dependence of the HBT radii at both energies was studied<sup>150,153</sup>. The azimuthal dependence of the  $K_\perp$ -integrated HBT radii  $R_o^2$ ,  $R_s^2$  and  $R_{os}^2$  was also analysed at both energies in minimum bias events<sup>153</sup>. So far, *STAR* determines the orientation of the reaction plane but it does not determine the direction of the impact parameter. Thus, the azimuthal dependence of  $R_{sl}^2$  and  $R_{ol}^2$  cannot be measured. Finally, a first study of three pion correlations indicates that the source is fully chaotic<sup>154</sup>.

*PHENIX* extends the results of *STAR* in a pseudo-rapidity window  $|\eta| < 0.35$  to higher  $K_\perp$ :  $0.2 < K_\perp < 1.2$  GeV/ $c$  at the lower and  $0.2 < K_\perp < 2$  GeV/ $c$  at the higher CMS energy. The particle momentum is measured by a drift chamber and a pad chamber. At  $\sqrt{s} = 130$  AGeV, correlation radii for both positive and negative identified pions are determined in three  $K_\perp$  bins<sup>147</sup>. For collisions at  $\sqrt{s} = 200$  AGeV, a much better statistics allowed to split the pairs into nine  $K_\perp$  bins<sup>148</sup>. The centrality dependence of the correlation radii was also studied. Correlation radii from kaon-kaon correlations did not show<sup>148</sup> a simple  $M_\perp$  scaling with the  $\pi\pi$  radii in contrast to expectations from certain hydrodynamically motivated parametrisations of the freeze-out state of the fireball<sup>24</sup>.

*PHOBOS* presented so far two sets of BP correlation radii for the 15% most central  $\sqrt{s} = 200$  AGeV Au+Au collisions. Data are for one  $K_\perp$  bin from 0.15 to 0.35 GeV/ $c$  and for  $0.2 < y < 1.5$ . One set was measured with  $\pi^+$  pairs, the other one with  $\pi^-$  pairs<sup>149</sup>.

## 4.5. Discussion of the data

### 4.5.1. Size and transverse momentum dependence of HBT radii

The out-, side-, and longitudinal HBT radius parameters vary typically around 5–6 fm at small transverse pair momentum  $K_\perp$  and decrease with increasing  $K_\perp$ . Their absolute size shows no significant dependence on beam energy (see Figs. 8 and 9). For data from the CERN SPS, the  $K_\perp$ -slope of the longitudinal radius parameter is steeper (see Fig. 6) while all radius

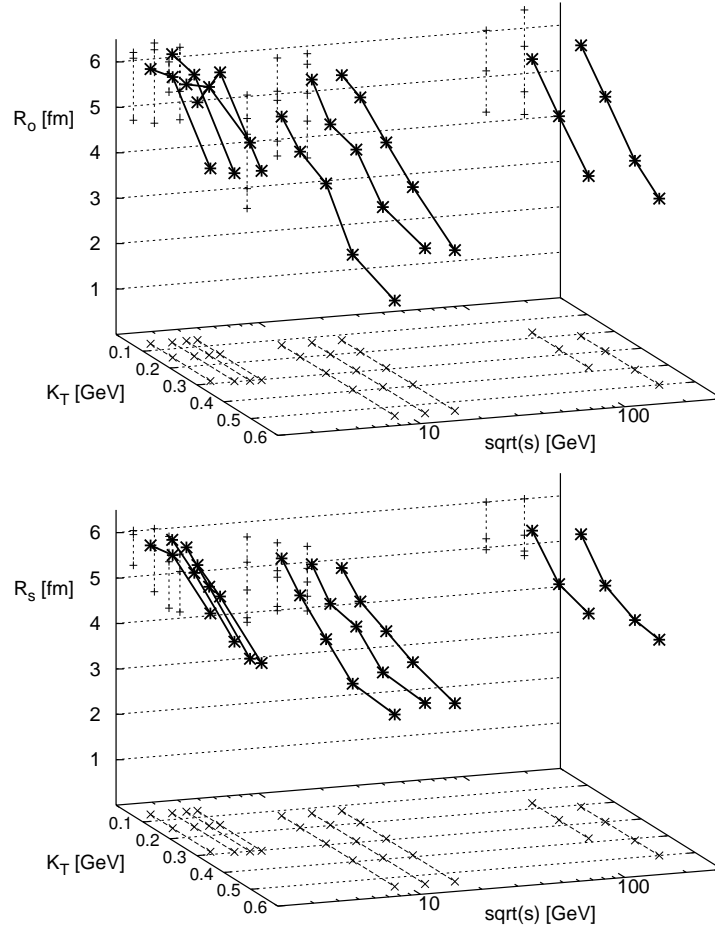


Fig. 8. The  $\sqrt{s}$  and  $K_\perp$  dependence of  $R_o$  and  $R_s$ . Data without error bars are summarised from E895<sup>114</sup> (Au+Au), NA45-CERES<sup>132</sup> (Pb+Au), and STAR  $\pi^+\pi^+$ <sup>150,153</sup> (Au+Au). STAR results for  $\sqrt{s} = 200$  AGeV are taken from transparencies shown at the Quark Matter 2002 conference.

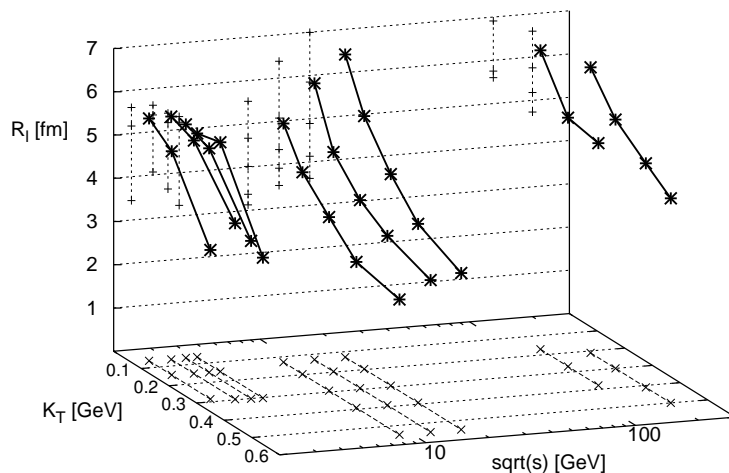


Fig. 9. The  $\sqrt{s}$  and  $K_{\perp}$  dependence of  $R_l$ . Data without error bars are summarised from E895<sup>114</sup>, NA45-CERES<sup>132</sup>, and STAR  $\pi^+\pi^+$ <sup>150,153</sup>. STAR results for  $\sqrt{s} = 200$  AGeV are taken from transparencies shown at the Quark Matter 2002 conference.

parameters measured at RHIC show approximately the same slope (see Fig. 7).

As explained in section 2.2.2, the HBT radius parameters of an expanding source correspond to the width of the  $K_{\perp}$ -dependent region of homogeneity. This is smaller than the width of the entire collision region. The  $K_{\perp}$ -slope of the HBT radii is a measure of the collective dynamical expansion. This picture can be illustrated by the pocket formulas (100), (101) and is supported by many model comparisons. If SPS data are fitted by a model with Gaussian transverse density distribution<sup>85,89</sup>, this leads to a radius of the entire collision region  $R \approx 7$  fm. To put this number into perspective, we relate the two-dimensional rms width of the collision region,  $r_{\text{rms}}^{\text{source}} = \sqrt{\langle \tilde{x}^2 + \tilde{y}^2 \rangle} = \sqrt{2} R \approx 10$  fm, to the two-dimensional rms widths of a cold lead nucleus. The hard sphere radius  $R_{\text{hs}}^{\text{A}} = 1.2 A^{1/3}$  fm is for lead  $R_{\text{hs}}^{\text{Pb}} = 7.1$  fm, and the corresponding two-dimensional transverse



rms width is  $r_{\text{rms}}^{\text{cold Pb}} = \sqrt{\langle \tilde{x}^2 + \tilde{y}^2 \rangle_{\text{Pb}}} = \sqrt{3/5} R_{\text{hs}}^{\text{Pb}} \approx 4.4$  fm. SPS data favour a model with a transverse box density profile<sup>89</sup> over a Gaussian density profile. The box radius is 10 – 12 fm. Irrespective of the transverse profile, one concludes that during the collision the system has expanded by a factor  $\approx 2$  from the transverse size of the overlapping cold lead nuclei to the transverse extension at freeze-out.

All available data are subject to significant systematic uncertainties. Additional uncertainties arise when comparing data from fixed target and collider experiments. In view of the rather mild changes of HBT radii between SPS and RHIC, this makes it difficult to assess to what extent the dynamical interpretation given above changes from SPS to RHIC. A first analysis of RHIC data<sup>26</sup> argues in favour of a more extended source with larger transverse flow, thus supporting the picture of a more vigorous transverse expansion at higher centre of mass energies.

#### 4.5.2. $R_o/R_s$

The main interest in the quotient or difference of the two transverse HBT radius parameters (15) and (16) lies in a model-dependent argument, that the emission duration  $\langle \tilde{t}^2 \rangle$  can be extracted from<sup>9,69</sup>

$$R_o^2(K) - R_s^2(K) \approx \beta_{\perp}^2 \langle \tilde{t}^2 \rangle. \quad (120)$$

This statement is based on two model-dependent assumptions. First, the term  $-2\beta_{\perp} \langle \tilde{x}\tilde{t} \rangle$  should be negligible compared to (120). This assumption, however, can be violated in models with strong expansion. Second, the difference  $\langle \tilde{x}^2 \rangle - \langle \tilde{y}^2 \rangle$  should be negligible compared to (120). This latter assumption can be violated at sufficiently high  $K_{\perp}$ , in particular in models for which particle emission peaks close to the surface due to dynamical or opacity effects.

Many model calculations predict  $R_o/R_s \gg 1$ . In particular, Rischke and Gyulassy<sup>73</sup> emphasised that this would be an unambiguous signal of an equation of state which is sufficiently soft in the phase transition region to result in a significantly delayed build-up of transverse expansion. This would result in a large lifetime effect,  $R_o/R_s \sim 1.5$ . In contrast, data indicate values  $R_o/R_s \lesssim 1.1$  even at RHIC, see Fig. 10. As mentioned in section 3.1, one can think of physics effects which result in  $R_o/R_s \lesssim 1$ . This issue is presently under study<sup>56,59</sup>.

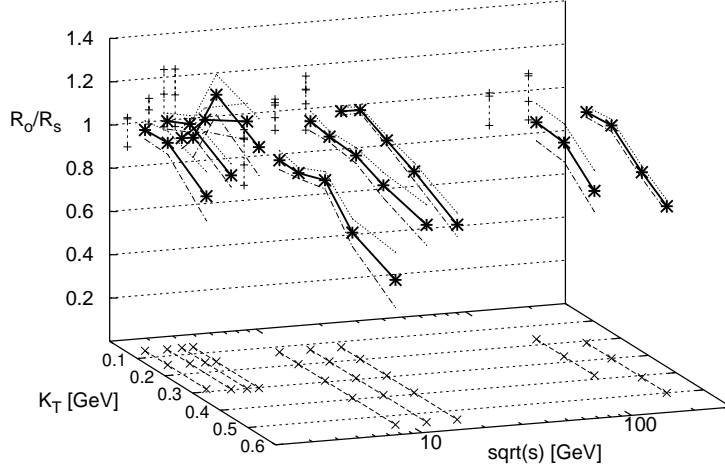


Fig. 10. The  $\sqrt{s}$  and  $K_{\perp}$  dependence of  $R_o/R_s$ . Data are summarised from E895<sup>114</sup>, NA45-CERES<sup>132</sup>, and STAR  $\pi^+\pi^+$ <sup>150,153</sup>. STAR results from  $\sqrt{s} = 200$  AGeV are taken from transparencies shown at the Quark Matter 2002 conference; their error bars may be underestimated.

#### 4.5.3. Average phase-space density

Idea and formalism: The spatial average of the phase-space density of pions at times later than freeze-out  $t_f$

$$\langle f \rangle(\mathbf{p}) = \frac{\int d^3x f^2(\mathbf{x}, \mathbf{p}, t > t_f)}{\int d^3x f(\mathbf{x}, \mathbf{p}, t > t_f)}, \quad (121)$$

can be expressed in terms of the observable one- and two-particle spectra<sup>11,109,33,89</sup>

$$\langle f \rangle(K_{\perp}, Y) = \frac{1}{\sqrt{\lambda}} \frac{1}{E} \frac{dN}{dY M_{\perp} dM_{\perp} d\Phi} \frac{1}{V_{\text{eff}}(K_{\perp}, Y)}, \quad (122)$$

$$V_{\text{eff}}(K_{\perp}, Y) = \left[ \int d^3\mathbf{q} (C(\mathbf{q}, \mathbf{K}) - 1) \right]^{-1}. \quad (123)$$

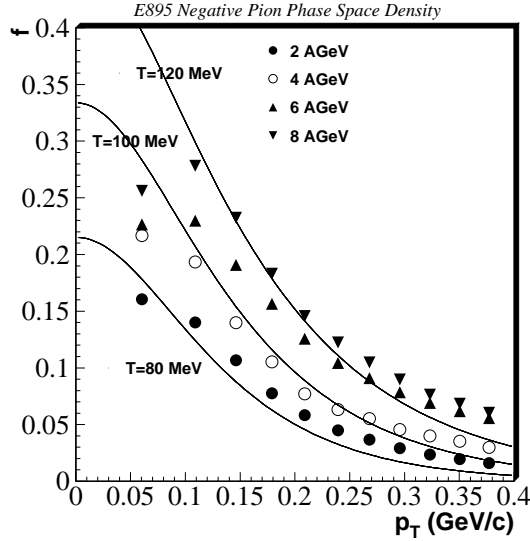


Fig. 11. Preliminary data on the average phase-space density as measured by the E895 Collaboration for different AGS projectile energies as a function of  $p_{\perp}$ <sup>116</sup>. The lines show Bose-Einstein distributions of given temperature. This does not account for the effects of expansion.

The phase-space density is determined by the average number of pions with given momentum (the *non*-invariant spectrum) divided by the volume in which they are contained. The factor  $\lambda^{-1/2}$  corrects for the “purity” of the sample: it ensures that only directly produced pions and not those coming from resonance decays are taken into account (see discussion at the end of section 2.1). As long as lifetime effects are small (which is consistent with all data measured so far, see Sec. 4.5.2), the volume is given by (123). For the Cartesian BP parametrisation, it takes the form

$$V_{\text{eff}}(K_{\perp}, Y) = \frac{1}{\pi^{3/2}} R_s(\mathbf{K}) \sqrt{R_o^2(\mathbf{K}) R_l^2(\mathbf{K}) - (R_{ol}^2(\mathbf{K}))^2}. \quad (124)$$

Thermal model as a reference: For reference, it is customary to compare the measured  $\langle f \rangle$  to that of a thermal distribution of a given temperature and chemical potential. Since  $\langle f \rangle$  is a spatial average, it averages for an expanding source over homogeneity regions which move relatively to the point of maximum emissivity. This leads to deviations from a naive Bose-Einstein phase-space density which for the case of a boost-invariant longitudinally

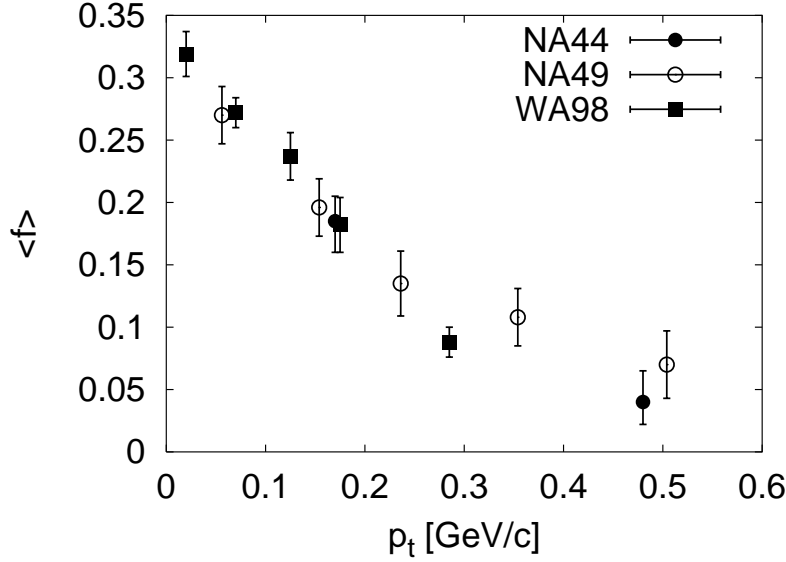


Fig. 12. The average pion phase-space density measured by NA44<sup>130</sup>, NA49<sup>33</sup>, and WA98<sup>146</sup> in 158 AGeV Pb+Pb collisions at mid-rapidity.

expanding pion source with transverse expansion can be written as<sup>90</sup>

$$\langle f \rangle(p_\perp) = \left( \sum_{n=1}^{\infty} A_n(p_\perp) \right) / \left( \sum_{n=2}^{\infty} (n-1) A_n(p_\perp) \right), \quad (125)$$

$$A_n(p_\perp) = 4\pi m_\perp \tau_f \int_0^\infty r dr e^{n[\mu(r)/T]} \times I_0(n p_\perp \sinh \zeta(r)/T) K_1(n m_\perp \cosh \zeta(r)/T). \quad (126)$$

Here, the transverse rapidity profile is characterised by  $\zeta(r)$  and the transverse density profile by  $\mu(r)/T$ . For illustration, the transverse geometry can be modelled e.g. by a box profile

$$[\text{box}] \quad \mu(r) = \begin{cases} \mu_B & \text{for } r \leq R_{\text{box}} \\ -\infty & \text{otherwise} \end{cases}, \quad (127)$$

or a Gaussian profile

$$[\text{Gauss}] \quad \mu(r) = \mu_G - T \frac{r^2}{2R_{\text{Gauss}}^2}. \quad (128)$$

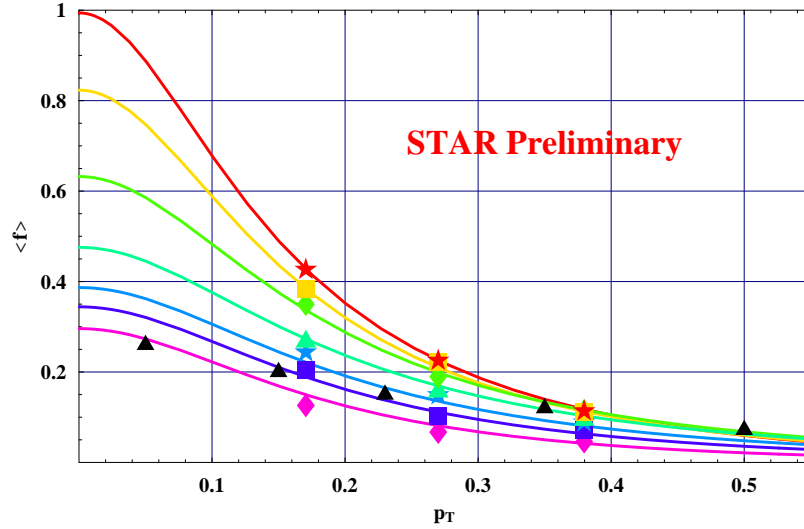


Fig. 13. The average pion phase-space density as measured by STAR Collaboration<sup>152</sup> for Au+Au collisions at  $\sqrt{s} = 130$  AGeV/c. Different symbols correspond to centralities (from top to bottom) 0-5%, 5-10%, 10-20%, 20-30%, 30-40%, 40-50%, and 50-80% of the total cross section. Curves are fits to eq. (125). The same thermal model also reproduces the single-particle spectrum. Triangles represent the NA49 data<sup>33</sup> for 158 AGeV Pb+Pb collisions at mid-rapidity.

The chemical potential  $\mu(r)$  introduced here are position-dependent and result in a non-uniform density profile;  $\mu_B$  or  $\mu_G$  are the values in the centre of the fireball. A certain spatial average of this chemical potential determines the particle multiplicities<sup>90</sup>. For comparison of the present formalism to AGS data, the assumption of boost-invariance entering (125) has to be modified by a rapidity cut-off.

Data: The average phase-space density was studied first by the E877 experiment for Au+Au collisions at the AGS<sup>109,110</sup> in the projectile fragmentation region where it was found to decrease with increasing rapidity. The E895 collaboration measured the average phase-space density at mid-rapidity at 2, 4, 6, and 8 AGeV and observed its increase with the collision energy<sup>116</sup> (Fig. 11).

At SPS energies there is an extensive compilation of phase-space densities for various collision systems based on data of the NA35/NA49 collaboration<sup>33</sup>, the NA44 measurements of S+S, S+Pb, and Pb+Pb

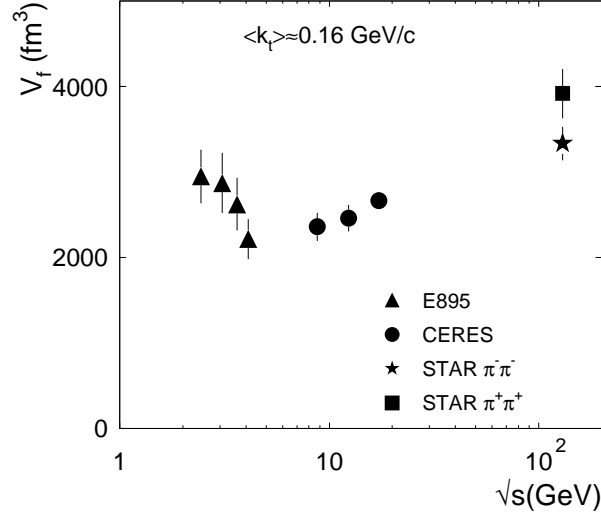


Fig. 14. Dependence of the “freeze-out volume”  $V_f = (2\pi)^{3/2} R_s^2 R_l$  on  $\sqrt{s}$ . Data are measured by E895<sup>114</sup>, CERES<sup>132</sup> and STAR<sup>150</sup> for low- $p_\perp$  pions at mid-rapidity.

collisions<sup>130</sup>, and the Pb+Pb data measured by WA98. For Pb+Pb collisions at 158 AGeV, the results of these experiments are mutually consistent, see Fig. 12.

At RHIC energy, preliminary data indicate that the average pion phase-space density is significantly higher than at SPS. Moreover, the STAR collaboration reported a strong dependence of the phase-space density on centrality<sup>152</sup> (Fig. 13). The origin of this increase, as well as the apparently different  $p_\perp$ -dependence of  $\langle f \rangle$  at RHIC and SPS, is currently under study.

#### 4.5.4. Energy and multiplicity dependence

Despite the weak dependence of HBT radius parameters on centre of mass energy, the volume  $V_f$  from which particles decouple shows an interesting non-monotonous behaviour, see Fig. 14. Here the volume is estimated as  $V_f \propto R_s^2 R_l$ . The radius  $R_o$  is not used in calculating  $V_f$  because it contains contributions from the temporal extent of the source, see eq. (16). The estimate  $V_f \propto R_s^2 R_l$  does not take into account the effects of the expansion on the HBT radii. Figure 14 shows that the volume decreases gradually

within the AGS energy range, reaches a minimum around the highest AGS energies and then increases monotonously by almost a factor 2 up to the highest RHIC energy.

At approximately fixed centre of mass energy at the SPS, the same freeze-out volume was found previously to grow linearly with the charged particle multiplicity per unit rapidity, see Fig. 15. Consistent with this finding is the centrality dependence of the freeze-out volume at SPS energies which grows linearly with the number of participants<sup>132</sup>. These two observations support the conjecture that freeze-out occurs at a fixed particle density. This is, however, contradicted by the non-monotonous energy dependence of  $V_f$ . A linear relation between freeze-out volume and particle multiplicity does not hold.

Particle density, and thus particle multiplicity is certainly important in characterising the freeze-out condition, since it affects the hadronic escape probability from the medium. However, chemical composition, collective expansion and the momentum of the escaping particle are other factors which determine this escape probability<sup>91</sup>. To illustrate this, one can consider e.g. the mean free path of a pion at freeze-out<sup>133</sup>

$$\lambda_{\text{mfp}}^{-1} = 2n_{p+\bar{p}}\sigma_{\pi N} + 3n_{\pi^-}\sigma_{\pi\pi} = 2\frac{N_{p+\bar{p}}}{V_f}\sigma_{\pi N} + 3\frac{N_{\pi^-}}{V_f}\sigma_{\pi\pi}. \quad (129)$$

While the freeze-out volume  $V_f$  and the numbers  $N_i$  of particles of species  $i$  contained in  $V_f$  both depend significantly on the centre of mass energy, the mean free path (129) is approximately  $\sqrt{s}$ -independent<sup>133</sup>.

To understand in more detail how the interplay of different properties of the collision region determines the freeze-out volume, a realistic freeze-out criterion is required. A good starting point is the particle escape probability from the hot and dense but rapidly expanding collision region<sup>29,79</sup>

$$\mathcal{P}(x, p, \tau) = \exp\left(-\int_{\tau}^{\infty} d\bar{\tau} \mathcal{R}(x + v\bar{\tau}, p)\right). \quad (130)$$

Here,  $v$  is the velocity of the escaping particle and  $\mathcal{R}(x, p)$  denotes the scattering rate which is defined as the inverse of the mean time between collisions for a particle at position  $x$  with momentum  $p$ . Freeze-out at different centre of mass energies is then assumed to occur when the probability  $\mathcal{P}$  reaches a characteristic value.

Recently, the scattering rate  $\mathcal{R}(x, p)$  was calculated for a full hadron resonance gas with chemical composition corresponding to SPS and RHIC

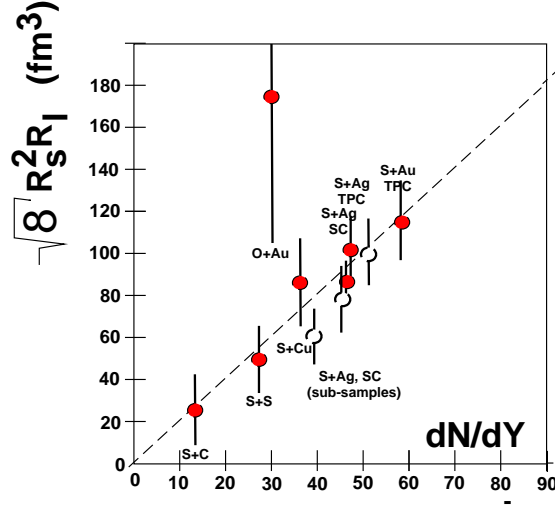


Fig. 15. The “freeze-out volume” ( $V_f \propto \sqrt{8} R_s^2 R_l$ ) as a function of the number of produced negative particles per unit of rapidity. Data are by NA35<sup>120</sup> for different S-induced reactions at 200 AGeV beam energy.

energies<sup>91</sup>. The main observation is that the scattering rate shows a significant momentum dependence suggesting that particles of different momenta are emitted at different times. This effect is neglected in hydrodynamic simulations which are based on the Cooper-Frye prescription<sup>22</sup> for freeze-out along a sharp three-dimensional hypersurface. Deviations from this Cooper-Frye prescription, i.e. freeze-out along finite four volumes may affect the transverse momentum slope of HBT radius parameters<sup>30</sup>, and the momentum dependence of the freeze-out volume. The role of a change in the chemical composition from SPS to RHIC was found to be relatively small in spite of the large increase of pion phase-space density (Fig. 13). This is a consequence of the small pion contribution to the total scattering rate, resulting from the comparatively small pion-pion cross-section. In contrast, collective transverse expansion gradients affect the freeze-out volume significantly. The reason is that an increase in the scattering rate at freeze-out can be compensated by stronger transverse flow gradients which lead to a faster density decrease in the collision region thus keeping the opacity integral in the exponent of (130) constant. The possible effect of



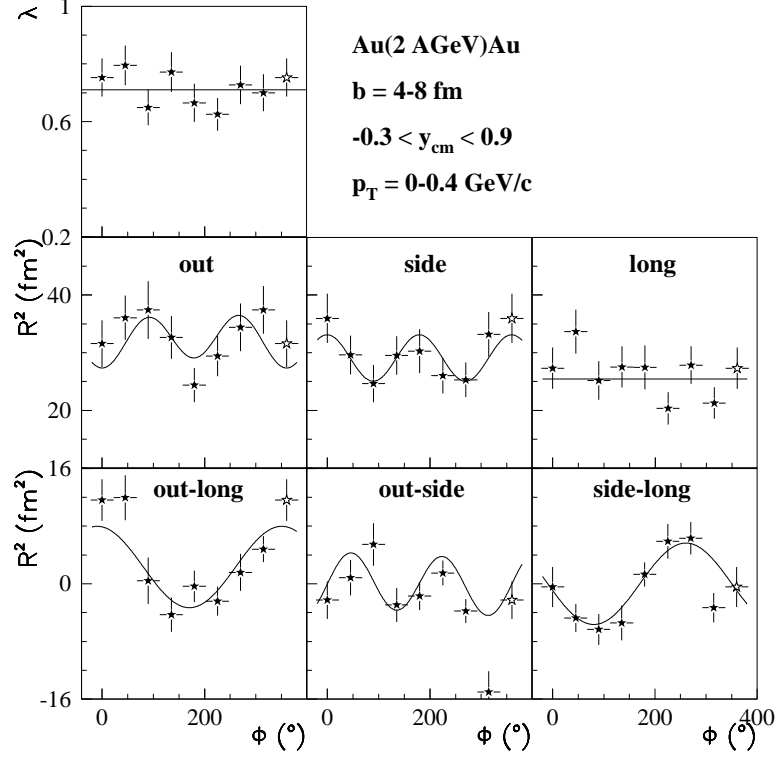


Fig. 16. Azimuthal dependence of HBT radius parameters as published by the E895 Collaboration<sup>113</sup> for Au+Au collisions at 2 AGeV. Curves correspond to a static source ( $\langle t^2 \rangle = 0$ ) according to the equations (51)-(56).

the flow gradients on the  $\sqrt{s}$ -dependence of the freeze-out volume (Fig. 14) remains to be studied.

#### 4.5.5. Azimuthal dependence of HBT radius parameters

Two years ago, the first measurements of the  $\Phi$ -dependence of HBT radius parameters were published by the E895 Collaboration<sup>113</sup> for beam energies of 2, 4 and 6 AGeV in semi-peripheral Au+Au collisions at the AGS. Results at all three energies show a sizeable first order harmonics in the

$\Phi$ -dependence of  $R_{ol}^2$  and  $R_{sl}^2$ , and comparatively small second order harmonics in the fully transverse HBT radii  $R_o^2$ ,  $R_s^2$  and  $R_{os}^2$ . The longitudinal radius parameter and the intercept  $\lambda$  are consistent with a  $\Phi$ -independent ansatz. According to (59), the first order harmonics allow to reconstruct the angle  $\Theta$  by which the emission ellipsoid is tilted out of the beam axis, see Fig. 5. At lower AGS energies, this angle is with  $\Theta \approx 30^\circ$  surprisingly large. This value is consistent with RQMD transport model simulations<sup>57</sup>. Interestingly, the spatial tilt is found to point in the direction opposite to the directed flow in momentum space. This indicates that at lower AGS energies pion reflection from the bulk of the matter rather than pion absorption by this matter is at the root of the observed direct flow signal.

With increasing centre of mass energy, a longitudinally approximately boost-invariant region develops around mid-rapidity. As a consequence, the tilt angle  $\Theta$  of the emission ellipsoid is expected to decrease with increasing  $\sqrt{s}$ . However, there is so far no measurement of  $R_{ol}^2$  and  $R_{sl}^2$  at higher energies, which would be required to establish this effect experimentally.

The  $\Phi$ -dependence of the fully transverse radius parameters  $R_o^2$ ,  $R_{os}^2$  and  $R_s^2$  is easier to measure than that of  $R_{ol}^2$  and  $R_{sl}^2$ : while the former require the event-wise reconstruction of the orientation of the reaction plane, the latter require in addition the direction in which the impact parameter points. Due to this complication, at RHIC first preliminary data are available for the fully transverse radius parameters only<sup>153</sup>. These data are expected to contain information about whether the spatial orientation of the source at freeze-out is in-plane or out-of-plane. However, statistical and systematic uncertainties in these preliminary data are still too large to draw conclusions. A significant improvement in statistics is expected within the next run.

## Acknowledgements

We are indebted to many colleagues for giving helpful informations. Thanks go in particular to Jan Pišút for a critical reading of the manuscript. We thank Giuseppe Bruno, John Cramer, Mike Lisa, and Piotr Skowroński for their comments to the manuscript. We profited from discussions with Harry Appelshäuser, Ulrich Heinz, and Mike Lisa. We are also very grateful to Harry Appelshäuser, Giuseppe Bruno, John Cramer, Peter Filip, Mike Lisa, Michael Murray, Laurent Rosselet, and Peter Seyboth who provided us with some of the data reviewed here.

## References

Theoretical papers:

1. J. Aichelin, Nucl. Phys. A **617** (1997) 510.
2. S. V. Akkelin and Y. M. Sinyukov, Z. Phys. C **72** (1996) 501.
3. S. V. Akkelin, P. Braun-Munzinger and Y. M. Sinyukov, Nucl. Phys. A **710** (2002) 439.
4. D. Anchishkin, U. W. Heinz and P. Renk, Phys. Rev. C **57** (1998) 1428.
5. H. W. Barz, Phys. Rev. C **53** (1996) 2536.
6. S. A. Bass *et al.*, Prog. Part. Nucl. Phys. **41** (1998) 225.
7. G. Baym and P. Braun-Munzinger, Nucl. Phys. A **610** (1996) 286C.
8. G. F. Bertsch, M. Gong and M. Tohyama, Phys. Rev. C **37** (1988) 1896.
9. G. F. Bertsch, Nucl. Phys. A **498** (1989) 173C.
10. G. F. Bertsch, P. Danielewicz and M. Herrmann, Phys. Rev. C **49** (1994) 442.
11. G. F. Bertsch, Phys. Rev. Lett. **72** (1994) 2349 [Erratum-ibid. **77** (1994) 789].
12. D. H. Boal, C. K. Gelbke and B. K. Jennings, Rev. Mod. Phys. **62** (1990) 553.
13. J. Bolz, U. Ornik, M. Plümer, B. R. Schlei and R. M. Weiner, Phys. Rev. D **47** (1993) 3860.
14. M. G. Bowler, Phys. Lett. B **270** (1991) 69.
15. D. A. Brown and P. Danielewicz, Phys. Rev. C **57** (1998) 2474.
16. D. A. Brown and P. Danielewicz, Phys. Rev. C **64** (2001) 014902.
17. S. Chapman and U. W. Heinz, Phys. Lett. B **340** (1994) 250.
18. S. Chapman, P. Scotto and U. W. Heinz, Phys. Rev. Lett. **74** (1995) 4400.
19. S. Chapman, P. Scotto and U. W. Heinz, Heavy Ion Phys. **1** (1995) 1.
20. S. Chapman, J. R. Nix and U. W. Heinz, Phys. Rev. C **52** (1995) 2694.
21. G. Cocconi, Phys. Lett. B **49** (1974) 459.
22. F. Cooper and G. Frye, Phys. Rev. D **10** (1974) 186.
23. T. Csörgő, B. Lörstad and J. Zimányi, Z. Phys. C **71** (1996) 491.
24. T. Csörgő and B. Lörstad, Phys. Rev. C **54** (1996) 1390.
25. T. Csörgő, arXiv:hep-ph/0001233.
26. T. Csörgő and A. Ster, arXiv:nucl-th/0207016.
27. G. Goldhaber, S. Goldhaber, W. Y. Lee and A. Pais, Phys. Rev. **120** (1960) 300.
28. P. Grassberger, Nucl. Phys. B **120** (1977) 231.
29. F. Grassi, Y. Hama and T. Kodama, Z. Phys. C **73**, 153 (1996).
30. F. Grassi, Y. Hama, S. S. Padula and O. J. Socolowski, Phys. Rev. C **62** (2000) 044904.
31. M. Gyulassy, S. K. Kauffmann and L. W. Wilson, Phys. Rev. C **20** (1979) 2267.
32. M. Gyulassy and S. K. Kauffmann, Nucl. Phys. A **362** (1981) 503.

33. D. Ferenc, U. W. Heinz, B. Tomášik, U. A. Wiedemann and J. G. Cramer, Phys. Lett. B **457** (1999) 347.
34. R. Hanbury Brown and R. Q. Twiss, Phil. Mag. **45** (1954) 663.
35. R. Hanbury Brown and R. Q. Twiss, Nature **178** (1956) 1046.
36. U. W. Heinz, B. Tomášik, U. A. Wiedemann and Y. F. Wu, Phys. Lett. B **382** (1996) 181.
37. U. W. Heinz and B. V. Jacak, Ann. Rev. Nucl. Part. Sci. **49** (1999) 529.
38. U. W. Heinz and P. F. Kolb, arXiv:hep-ph/0204061.
39. U. W. Heinz, A. Hummel, M. A. Lisa and U. A. Wiedemann, Phys. Rev. C **66** (2002) 044903.
40. H. Heiselberg and A. P. Vischer, Eur. Phys. J. C **1** (1998) 593.
41. H. Heiselberg, Phys. Rev. Lett. **82** (1999) 2052.
42. H. Heiselberg and A. M. Levy, Phys. Rev. C **59** (1999) 2716.
43. M. Herrmann and G. F. Bertsch, Phys. Rev. C **51** (1995) 328.
44. T. Hirano, K. Morita, S. Muroya and C. Nonaka, Phys. Rev. C **65** (2002) 061902.
45. T. J. Humanic, Phys. Rev. C **50** (1994) 2525.
46. T. J. Humanic, Phys. Rev. C **53** (1996) 901.
47. T. J. Humanic, arXiv:nucl-th/0205053.
48. W. Kittel, Acta Phys. Polon. B **32** (2001) 3927.
49. P. F. Kolb, J. Sollfrank and U. W. Heinz, Phys. Rev. C **62** (2000) 054909.
50. S. E. Koonin, Phys. Lett. B **70** (1977) 43.
51. G. I. Kopylov and M. I. Podgoretsky, Sov. J. Nucl. Phys. **15** (1972) 219 [Yad. Fiz. **15** (1972) 392].
52. G. I. Kopylov and M. I. Podgoretsky, Sov. J. Nucl. Phys. **18** (1974) 336 [Yad. Fiz. **18** (1974) 656].
53. R. Lednický and V. L. Lyuboshits, Sov. J. Nucl. Phys. **35** (1982) 770 [Yad. Fiz. **35** (1982) 1316].
54. R. Lednický and V. L. Lyuboshits, Heavy Ion Phys. **3** (1996) 93.
55. R. Lednický, V. L. Lyuboshits, B. Erazmus and D. Nouais, Phys. Lett. B **373** (1996) 30.
56. Z.W. Lin, C.M. Ko and S. Pal, arXiv:nucl-th/0204054.
57. M. A. Lisa, U. W. Heinz and U. A. Wiedemann, Phys. Lett. B **489** (2000) 287.
58. A. N. Makhlin and Y. M. Sinyukov, Z. Phys. C **39** (1988) 69.
59. L. McLerran and S. S. Padula, arXiv:nucl-th/0205028.
60. D. Molnár and M. Gyulassy, arXiv:nucl-th/0211017.
61. K. Morita, S. Muroya, H. Nakamura and C. Nonaka, Phys. Rev. C **61** (2000) 034904.
62. K. Morita, S. Muroya, C. Nonaka and T. Hirano, Phys. Rev. C **66** (2002) 054904.
63. J. Y. Ollitrault, Nucl. Phys. A **638** (1998) 195C.
64. M. I. Podgoretsky, Sov. J. Nucl. Phys. **37** (1983) 272 [Yad. Fiz. **37** (1983) 455].

65. A. M. Poskanzer and S. A. Voloshin, Phys. Rev. C **58** (1998) 1671.
66. S. Pratt, Phys. Rev. Lett. **53** (1984) 1219.
67. S. Pratt, Phys. Rev. D **33** (1986) 72.
68. S. Pratt, Phys. Rev. D **33** (1986) 1314.
69. S. Pratt, T. Csörgő and J. Zimányi, Phys. Rev. C **42** (1990) 2646.
70. see S. Pratt's web page:  
<http://www.nsc1.msu.edu/~pratt/freecodes/crab/home.html>.
71. R. L. Ray, Phys. Rev. C **57** (1998) 2523.
72. D. H. Rischke and M. Gyulassy, Nucl. Phys. A **597** (1996) 701.
73. D. H. Rischke and M. Gyulassy, Nucl. Phys. A **608** (1996) 479.
74. B. R. Schlei, U. Ornik, M. Plumer and R. M. Weiner, Phys. Lett. B **293** (1992) 275.
75. B. R. Schlei, Phys. Rev. C **55** (1997) 954.
76. B. R. Schlei, D. Strottman, J. P. Sullivan and H. W. van Hecke, Eur. Phys. J. C **10** (1999) 483.
77. E. V. Shuryak, Phys. Lett. B **44**, 387 (1973).
78. Y. Sinyukov, R. Lednický, S. V. Akkelin, J. Pluta and B. Erasmus, Phys. Lett. B **432** (1998) 248.
79. Y. M. Sinyukov, S. V. Akkelin and Y. Hama, Phys. Rev. Lett. **89** (2002) 052301.
80. S. Soff, S. A. Bass and A. Dumitru, Phys. Rev. Lett. **86** (2001) 3981.
81. S. Soff, S. A. Bass, D. H. Hardtke and S. Y. Panitkin, Phys. Rev. Lett. **88** (2002) 072301.
82. S. Soff, arXiv:hep-ph/0202240.
83. H. Sorge, H. Stöcker and W. Greiner, Nucl. Phys. A **498** (1989) 567C.
84. H. Sorge, H. Stöcker and W. Greiner, Annals Phys. **192** (1989) 266.
85. A. Ster, T. Csörgő and B. Lörstad, Nucl. Phys. A **661** (1999) 419.
86. J. P. Sullivan *et al.*, Phys. Rev. Lett. **70** (1993) 3000.
87. B. Tomášik and U. W. Heinz, Eur. Phys. J. C **4** (1998) 327.
88. B. Tomášik and U. W. Heinz, Acta Phys. Slov. **49** (1999) 251.
89. B. Tomášik, U. A. Wiedemann and U. W. Heinz, arXiv:nucl-th/9907096.
90. B. Tomášik and U. W. Heinz, Phys. Rev. C **65** (2002) 031902.
91. B. Tomášik and U. A. Wiedemann, arXiv:nucl-th/0207074.
92. S. A. Voloshin and W. E. Cleland, Phys. Rev. C **53** (1996) 896.
93. S. A. Voloshin and W. E. Cleland, Phys. Rev. C **54** (1996) 3212.
94. S. Voloshin, R. Lednický, S. Panitkin and N. Xu, Phys. Rev. Lett. **79** (1997) 4766.
95. U. A. Wiedemann, P. Scotto and U. W. Heinz, Phys. Rev. C **53** (1996) 918.
96. U. A. Wiedemann and U. W. Heinz, Phys. Rev. C **56** (1997) 3265.
97. U. A. Wiedemann and U. W. Heinz, Phys. Rev. C **56** (1997) 610.
98. U. A. Wiedemann, Phys. Rev. C **57** (1998) 266.
99. U. A. Wiedemann, D. Ferenc and U. W. Heinz, Phys. Lett. B **449** (1999) 347.
100. U. A. Wiedemann and U. W. Heinz, Phys. Rept. **319** (1999) 145.

- 101. Y. F. Wu, U. W. Heinz, B. Tomášik and U. A. Wiedemann, Eur. Phys. J. C **1** (1998) 599.
- 102. F. B. Yano and S. E. Koonin, Phys. Lett. B **78** (1978) 556.
- 103. W. A. Zajc *et al.*, Phys. Rev. C **29** (1984) 2173.
- 104. W. A. Zajc, Phys. Rev. D **35** (1987) 3396.
- 105. D. Zschesche, S. Schramm, H. Stöcker and W. Greiner, Phys. Rev. C **65** (2002) 064902.

Experimental papers:

- 106. V. Cianciolo [E802 Collaboration], Nucl. Phys. A **590** (1995) 459C.
- 107. L. Ahle [E802 Collaboration], Phys. Rev. C **66** (2002) 054906.
- 108. J. Barrette *et al.* [E814 Collaboration.], Phys. Lett. B **333** (1994) 33.
- 109. D. Miśkowiec *et al.* [E877 Collaboration], Nucl. Phys. A **610** (1996) 227C.
- 110. J. Barrette *et al.* [E877 Collaboration], Phys. Rev. Lett. **78** (1997) 2916.
- 111. J.P. Wessels *et al.* [E877 Collaboration], Nucl. Phys. A **638** (1998) 69.
- 112. G. Rai *et al.*, IEEE Trans. Nucl. Sci. **37** (1990) 56.
- 113. M. A. Lisa *et al.* [E895 Collaboration], Phys. Lett. B **496** (2000) 1.
- 114. M.A. Lisa *et al.* [E895 Collaboration], Phys. Rev. Lett. **84** (2000) 2798.
- 115. S. Y. Panitkin *et al.* [E895 Collaboration], Phys. Rev. Lett. **87** (2001) 112304.
- 116. M. A. Lisa *et al.* [E895 Collaboration], Nucl. Phys. A **698** (2002) 185.
- 117. B. Holzmann for the E917 Collaboration, *Heavy Ion Physics from Bevalac to RHIC*, ed. by R. Seto, (World Scientific, Singapore, 1999).
- 118. A. Bamberger *et al.* [NA35 Collaboration], Phys. Lett. B **203** (1988) 320.
- 119. T. J. Humanic *et al.* [NA35 Collaboration], Z. Phys. C **38** (1988) 79.
- 120. T. Alber *et al.* [NA35 Collaboration], Z. Phys. C **66** (1995) 77.
- 121. T. Alber *et al.* [NA35 Collaboration.], Phys. Rev. Lett. **74** (1995) 1303.
- 122. T. Alber [NA35 and NA49 Collaborations], Nucl. Phys. A **590** (1995) 453C.
- 123. H. Boggild *et al.* [NA44 Collaboration], Phys. Lett. B **302** (1993) 510 [Erratum-ibid. B **306** (1993) 418].
- 124. H. Beker *et al.* [NA44 Collaboration], Z. Phys. C **64** (1994) 209.
- 125. H. Boggild *et al.* [NA44 Collaboration], Phys. Lett. B **349** (1995) 386.
- 126. H. Beker *et al.* [NA44 Collaboration], Phys. Rev. Lett. **74** (1995) 3340.
- 127. K. Kaimi *et al.* [NA44 Collaboration], Z. Phys. C **75** (1997) 619.
- 128. I. G. Bearden *et al.* [NA44 Collaboration], Phys. Rev. C **58** (1998) 1656.
- 129. H. Boggild *et al.* [NA44 Collaboration], Phys. Lett. B **455** (1999) 77.
- 130. M. Murray and B. Holzer, Phys. Rev. C **63** (2001) 054901.
- 131. I. G. Bearden *et al.* [NA44 Collaboration], Phys. Rev. Lett. **87** (2001) 112301.
- 132. D. Adamová *et al.* [NA45 CERES Collaboration], arXiv:nucl-ex/0207005.
- 133. D. Adamová *et al.* [NA45 CERES Collaboration], arXiv:nucl-ex/0207008.
- 134. H. Appelshäuser *et al.* [NA49 Collaboration], Eur. Phys. J. C **2** (1998) 661.
- 135. R. Ganz *et al.* [NA49 Collaboration], arXiv:nucl-ex/9808006.

- 136. R. Ganz [NA49 Collaboration], Nucl. Phys. A **661** (1999) 448.
- 137. P. Seyboth *et al.* [NA49 Collaboration], arXiv:hep-ex/0206046.
- 138. C. Blume for the NA49 Collaboration, arXiv:nucl-ex/0208020, (Proceedings of Quark Matter 2002, to be published in Nucl. Phys. A), see also transparencies at <http://alice-france.in2p3.fr/qm2002/Transparencies/19Plenary/Blume.pdf>.
- 139. S. V. Afanasiev *et al.* [NA49 Collaboration], arXiv:nucl-ex/0210018.
- 140. R. Albrecht *et al.* [WA80 Collaboration], Z. Phys. C **53** (1992) 225.
- 141. R. Albrecht *et al.* [WA80 Collaboration], Phys. Rev. C **50** (1994) 1048.
- 142. T. C. Awes *et al.* [WA80 Collaboration], Z. Phys. C **69** (1995) 67.
- 143. F. Antinori *et al.* [WA97 Collaboration], J. Phys. G **27** (2001) 2325.
- 144. M. M. Aggarwal *et al.* [WA98 Collaboration], Eur. Phys. J. C **16** (2000) 445.
- 145. M. M. Aggarwal *et al.* [WA98 Collaboration], Phys. Rev. Lett. **85** (2000) 2895.
- 146. M. M. Aggarwal [WA98 Collaboration], arXiv:nucl-ex/0210002.
- 147. K. Adcox *et al.* [PHENIX Collaboration], Phys. Rev. Lett. **88** (2002) 192302.
- 148. A. Enokizono for the PHENIX Collaboration, arXiv:nucl-ex/0209026, (Proceedings of Quark Matter 2002, to be published in Nucl. Phys. A).
- 149. S. Manly for the PHOBOS Collaboration, arXiv:nucl-ex/0210036, (Proceedings of Quark Matter 2002, to be published in Nucl. Phys. A).
- 150. C. Adler *et al.* [STAR Collaboration], Phys. Rev. Lett. **87** (2001) 082301.
- 151. F. Retière [STAR Collaboration], arXiv:nucl-ex/0111013.
- 152. L. Ray for the STAR Collaboration, arXiv:nucl-ex/0211030 (Proceedings of Quark Matter 2002, to be published in Nucl. Phys. A).
- 153. M. López Noriega for the STAR Collaboration, arXiv:nucl-ex/0210031 (Proceedings of Quark Matter 2002, to be published in Nucl. Phys. A).
- 154. R. Willson for the STAR Collaboration, arXiv:nucl-ex/0211026 (Proceedings of Quark Matter 2002, to be published in Nucl. Phys. A).